A well-balanced Runge-Kutta discontinuous Galerkin method for multilayer shallow water equations with non-flat bottom topography

Nouh Izem[1,*] Mohammed Seaid[2,†]

[1] *Laboratory of Engineering Sciences LabSI, Faculty of Science, Ibn Zohr University Agadir, Morocco*
[2] *Department of Engineering, University of Durham, South Road, Durham DH1 3LE, UK*

Abstract

A well-balanced Runge-Kutta discontinuous Galerkin method is presented for the numerical solution of multilayer shallow water equations with mass exchange and non-flat bottom topography. The governing equations are reformulated as a nonlinear system of conservation laws with differential source forces and reaction terms. Coupling between the flow layers is accounted for in the system using a set of exchange relations. The considered well-balanced Runge-Kutta discontinuous Galerkin method is a locally conservative finite element method whose approximate solutions are discontinuous across the inter-element boundaries. The well-balanced property is achieved using a special discretization of source terms that depends on the nature of hydrostatic solutions along with the Gauss-Lobatto-Legendre nodes for the quadrature used in the approximation of source terms. The method can also be viewed as a high-order version of upwind finite volume solvers and it offers attractive features for the numerical solution of conservation laws for which standard finite element methods fail. To deal with the source terms we also implement a high-order splitting operator for the time integration. The accuracy of the proposed Runge-Kutta discontinuous Galerkin method is examined for several examples of multilayer free-surface flows over both flat and non-flat beds. The performance of the method is also demonstrated by comparing the results obtained using the proposed method to those obtained using the incompressible hydrostatic Navier-Stokes equations and a well-established kinetic method. The proposed method is also applied to solve a recirculation flow problem in the Strait of Gibraltar.

Keywords. Discontinuous Galerkin method; Well-balanced discretization; Runge-Kutta scheme; Multilayer shallow water equations; Free-surface flows; Mass exchange; Wind-driven flows; Strait of Gibraltar

1 Introduction

The incompressible Navier-Stokes equations have been well established as accurate tools for modelling and simulating water flows, see [10, 47] among others. However, for free-surface flows, these equations become difficult to numerically solve mainly due to the hydrostatic assumption on the pressure and the presence of moving boundaries within the flow domain. On the other hand, assuming that the pressure is hydrostatic and the vertical scale is far smaller than the horizontal scale, the shallow water equations can be derived by depth-averaging the three-dimensional Navier-Stokes equations, see for instance [1]. Indeed, shallow water equations have been widely used in modelling many engineering applications in free-surface flows and hydraulics such as tides in coastal regions, floods in rivers, water flows in reservoir, and open channel flows among others, see for example [33, 43]. However, because these equations are derived based on depth-averaged procedures, the vertical velocity component is not resolved in these models and the

[*] n.izem@uiz.ac.ma
[†] m.seaid@durham.ac.uk

bed friction is derived only in terms of the mean flow velocity rather than the velocity near the bottom. Hence, the three-dimensional modeling of hydraulics is required for an accurate representation of the flow structures, especially for recirculation flows and for solution of near-field problems involving sediment transport in rivers and coastal engineering. In the recent years, research in shallow water flows has been shifted to overcome the shortcomings of this type of modeling namely, the use of single velocity profile for the entire depth of the water flow. This has conducted to the introduction of multilayer shallow water equations for geophysical free-surface flows. For example, two-layer shallow water equations have been proposed to model immiscible fluids in [16, 24]. More recently, multilayer shallow water equations with mass exchange terms have been studied in [6, 13, 4, 11] among others. The governing equations in these multilayer models have been derived using a P_0 finite element discretization of the vertical velocity in the three-dimensional incompressible Navier-Stokes equations. This class of multilayer shallow water equations avoid the computationally demanding methods needed to solve the three-dimensional incompressible Navier-Stokes equations with free-surface but at the same time providing stratified flow velocities since the pressure distribution is still assumed to be hydrostatic. In the current study, the free-surface flow problem is approximated as a layered system made of multiple shallow water systems of different water heights but coupled through mass-exchange terms between the embedded layers. These water layers may also differ in terms of density, viscosity, compressibility and potential for mixing among others. Recently, multilayer shallow water equations have been subject of various research studies and have been used for modelling a variety of free-surface flows such as estuaries, bays and other nearshore regions where water free-surface flows interact with the bed geometry and wind shear stresses, see for example [6, 13, 4].

The Runge-Kutta Discontinuous Galerkin (RKDG) method belongs to a class of finite element methods which uses discontinuous piecewise polynomials for the numerical solution and for the test functions whereas, the time integration is performed using an explicit third-order Runge-Kutta scheme. During the recent years, the RKDG method has been investigated for many practical applications in engineering, see [8] for a review and further references are therein. The RKDG method has also been implemented for solving the standard single-layer shallow water equations, see for instance [2, 12, 25]. Extension of the RKDG method for two-layer shallow water equation of immiscible fluids has also been presented in [21, 20]. Based on the results reported in these references and other in the literature, the RKDG method has proven to offer (i) the ability to preserve the advantages of the conventional finite element method to handle complicated geometries, (ii) the implementation of mesh adaptation without need of continuity assumptions on the conformity of the finite elements, (iii) the possibility to increase the accuracy of the overall method by increasing the degree of the approximating polynomials locally, thus allowing an efficient p-adaptivity for each element independently of its neighbors (iv) the efficient parallel implementation, since each element solution communicates with its immediate neighbors only regardless of the order of accuracy, and (v) the capability to handle calculations of gradually varying flows as well as rapidly varying flows over both flat and non-flat beds. In the present work, using the hydrostatic reconstruction, we develop a well-balanced RKDG method that is efficient and high-order accurate to solve the multilayer shallow water equations without relying on the Riemann-solver based finite volume methods. This objective is achieved by using a second-order splitting operator for the time integration combined with a hydrostatic reconstruction to reconstruct well-balanced discretization of flux gradients and source terms in the system. It should be stressed that hydrostatic reconstruction has been first developed in [5] for single-layer shallow water equations and applied later to free-surface water flows in [32] and to blood flows in [27]. To the best of our knowledge, solving multilayer shallow water equations with exchange terms using the RKDG method is presented for the first time. Several numerical examples are presented to demonstrate the performance of the proposed RKDG method to accurately solve the multilayer shallow water equations. We verify the model capability of calculating vertical distributions of the water velocity for the multilayer shallow water flows over both flat and non-flat beds. We also compare the results obtained using the RKDG method to the results obtained using the incompressible Navier-Stokes equations for a dam-break problem. The performance of the proposed RKDG method for resolving recirculation flows in the Strait of Gibraltar is also investigated. Numerical results presented

in the current study demonstrate high resolution of the RKDG method and confirm its capability to provide highly accurate solutions for multilayer free-surface flows with mass exchange.

This paper is organized as follows. In Section 2 we present a brief description of the governing equations for multilayer free-surface flows with mass exchange. Formulation of the Runge-Kutta discontinuous Galerkin method for solving these equations is discussed in Section 3. This section includes the finite element method for space discretization and the Runge-Kutta scheme for the time integration. Numerical results and examples are presented in Section 4. Section 5 contains conclusions.

2 Equations for multilayer free-surface flows

Using a vertical P_0-type discretization of the horizontal velocity, the equations for three-dimensional hydrostatic incompressible Navier-Stokes equations with free surface yields the so-called multilayer shallow water equations, see [6, 13] for detailed derivations of these equations. The water exchange between the layers is accounted for in these equations through source terms included in the momentum equations. Thus, the governing equations are defined as

$$\begin{aligned} \frac{\partial H}{\partial t} + \sum_{\alpha=1}^{M} \frac{\partial}{\partial x}\left(l_\alpha H u_\alpha\right) &= 0, \\ \frac{\partial}{\partial t}\left(l_\alpha H u_\alpha\right) + \frac{\partial}{\partial x}\left(l_\alpha H u_\alpha^2 + \frac{1}{2} g l_\alpha H^2\right) &= -g l_\alpha H \frac{\partial Z}{\partial x} + \mathcal{S}_\alpha^u + \mathcal{S}_\alpha^\mu + \mathcal{S}_\alpha^b + \mathcal{S}_\alpha^w, \end{aligned} \tag{1}$$

where $u_\alpha(x,t)$ is the local water velocity for the αth layer, $Z(x)$ is the topography of the flow domain, g is the gravitational acceleration, $H(x,t)$ is the water height of the whole flow system and l_α denotes the relative size of the αth layer satisfying the conditions

$$l_\alpha > 0, \qquad \sum_{\alpha=1}^{M} l_\alpha = 1.$$

The water height $h_\alpha(x,t)$ of the αth layer is defined as a fraction of the total water height by

$$\hbar_\alpha = l_\alpha H, \qquad \alpha = 1, \ldots, M,$$

where M is the total number of layers in the flow domain, see Figure 1 for an illustration. Note that the relative size l_α is prescribed a priori and all the layers are assumed to have the same water density. In (1), the source term $\mathcal{S}_\alpha^u$ is related to the momentum exchanges between the layers which is defined through the vertical P_0 discretization of the flow as

$$\mathcal{S}_\alpha^u = u_{\alpha+1/2} G_{\alpha+1/2} - u_{\alpha-1/2} G_{\alpha-1/2}, \tag{2}$$

with the mass exchange terms $G_{\alpha-1/2}$ and $G_{\alpha+1/2}$ are calculated by

$$G_{\alpha-1/2} = \begin{cases} 0, & \text{if} \quad \alpha = 1, \\ \displaystyle\sum_{\beta=1}^{\alpha-1} \left(\frac{\partial\left(\hbar_\beta u_\beta\right)}{\partial x} - l_\beta \sum_{\gamma=1}^{M} \frac{\partial\left(\hbar_\gamma u_\gamma\right)}{\partial x} \right), & \text{if} \quad \alpha = 2, 3 \ldots, M, \end{cases} \tag{3}$$

$$G_{\alpha+1/2} = \begin{cases} \displaystyle\sum_{\beta=1}^{\alpha} \left(\frac{\partial\left(\hbar_\beta u_\beta\right)}{\partial x} - l_\beta \sum_{\gamma=1}^{M} \frac{\partial\left(\hbar_\gamma u_\gamma\right)}{\partial x} \right), & \text{if} \quad \alpha = 1, 2, \ldots, M-1, \\ 0, & \text{if} \quad \alpha = M, \end{cases} \tag{4}$$

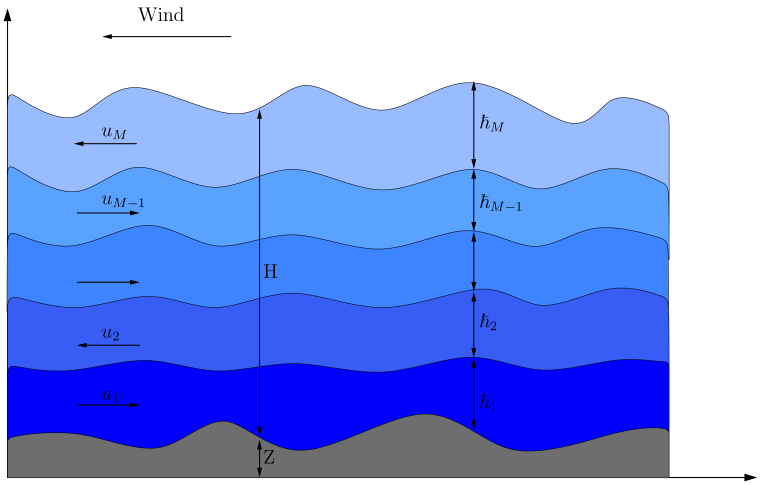

Figure 1: Schematic of a multilayer free-surface flow system.

and the interface velocities $u_{\alpha-1/2}$ and $u_{\alpha+1/2}$ are evaluated using an upwind procedure following the sign of the mass exchange terms (3) and (4) as

$$u_{\alpha-1/2} = \begin{cases} u_{\alpha-1}, & \text{if} \quad G_{\alpha-1/2} \geq 0, \\ u_{\alpha}, & \text{if} \quad G_{\alpha-1/2} < 0. \end{cases} \qquad u_{\alpha+1/2} = \begin{cases} u_{\alpha}, & \text{if} \quad G_{\alpha+1/2} \geq 0, \\ u_{\alpha+1}, & \text{if} \quad G_{\alpha+1/2} < 0. \end{cases} \tag{5}$$

The vertical kinematic eddy viscosity terms $\mathcal{S}_\alpha^\mu$ in (1) account for the friction between the neighboring layers as

$$\mathcal{S}_\alpha^\mu = \begin{cases} 2\nu \dfrac{u_2 - u_1}{(l_2 + l_1)\, H}, & \text{if} \quad \alpha = 1, \\ 2\nu \dfrac{u_{\alpha+1} - u_\alpha}{(l_{\alpha+1} + l_\alpha)\, H} - 2\nu \dfrac{u_\alpha - u_{\alpha-1}}{(l_\alpha + l_{\alpha-1})\, H}, & \text{if} \quad \alpha = 2, 3, \ldots, M-1, \\ -2\nu \dfrac{u_M - u_{M-1}}{(l_M + l_{M-1})\, H}, & \text{if} \quad \alpha = M, \end{cases} \tag{6}$$

where ν is the eddy viscosity. The external friction terms $\mathcal{S}_\alpha^b$ and $\mathcal{S}_\alpha^w$ in (1) are defined by

$$\mathcal{S}_\alpha^b = \begin{cases} -\dfrac{\tau_b}{\rho}, & \text{if} \quad \alpha = 1, \\ 0, & \text{if} \quad \alpha = 2, 3, \ldots, M, \end{cases} \qquad \mathcal{S}_\alpha^w = \begin{cases} 0, & \text{if} \quad \alpha = 1, 2, \ldots, M-1, \\ \dfrac{\tau_w}{\rho}, & \text{if} \quad \alpha = M, \end{cases} \tag{7}$$

with ρ is the water density, τ_b and τ_w are respectively, the bed shear stress and the shear of the blowing wind defined by the water velocity u_1 and the wind velocity w as

$$\tau_b = \rho C_b u_1 \left|u_1\right|, \qquad \tau_w = \rho C_w w \left|w\right|, \tag{8}$$

where C_b is the bed friction coefficient and C_w is the wind friction coefficient given by [38]

$$C_b = \frac{g n_b^2}{H^{1/3}}, \qquad C_w = \frac{\sigma^2 \rho_a}{H},$$

with n_b is the Manning roughness coefficient at the bed, w the wind velocity at 10 m above the water surface, σ^2 the wind stress coefficient and ρ_a the air density. It should be noted that in the multilayer

system (1), the internal friction term $\mathcal{S}_\alpha^\mu$ models the friction between neighboring layers, the bed-friction forcing term $\mathcal{S}_\alpha^b$ is acting only on the lower layer, and the wind-driven forcing term $\mathcal{S}_\alpha^w$ is acting only on the upper layer. More details on rigorous derivations of the multilayer shallow water system (1) from the three-dimensional incompressible Navier-Stokes equations can be found in [6, 13]. Note that the multilayer shallow water equations (1) can also be rearranged in a compact vector form as

$$\frac{\partial \mathbf{W}}{\partial t} + \frac{\partial \mathbf{F}(\mathbf{W})}{\partial x} = \mathbf{Q}(\mathbf{W}) + \mathbf{R}(\mathbf{W}), \tag{9}$$

where $\mathbf{W}$ is the vector of conserved variables, $\mathbf{F}$ the vector of flux functions, $\mathbf{Q}$ and $\mathbf{R}$ are the vector of source terms

$$\mathbf{W} = \begin{pmatrix} H \\ Hu_1 \\ Hu_2 \\ \vdots \\ Hu_M \end{pmatrix}, \qquad \mathbf{F}(\mathbf{W}) = \begin{pmatrix} \sum_{\alpha=1}^{M} l_\alpha H u_\alpha \\ Hu_1^2 + \frac{1}{2} g H^2 \\ Hu_2^2 + \frac{1}{2} g H^2 \\ \vdots \\ Hu_M^2 + \frac{1}{2} g H^2 \end{pmatrix}, \qquad \mathbf{Q}(\mathbf{W}) = \begin{pmatrix} 0 \\ -gH\frac{\partial Z}{\partial x} \\ -gH\frac{\partial Z}{\partial x} \\ \vdots \\ -gH\frac{\partial Z}{\partial x} \end{pmatrix},$$

$$\mathbf{R}(\mathbf{W}) = \begin{pmatrix} 0 \\ \frac{1}{l_1}\left(u_{3/2}G_{3/2} - \frac{\tau_b}{\rho} + 2\nu\frac{u_2 - u_1}{(l_2 + l_1)\,H}\right) \\ \frac{1}{l_2}\left(u_{5/2}G_{5/2} - u_{3/2}G_{3/2} + 2\nu\frac{u_3 - u_2}{(l_3 + l_2)\,H} - 2\nu\frac{u_2 - u_1}{(l_2 + l_1)\,H}\right) \\ \vdots \\ \frac{1}{l_{M-1}}\left(u_{M-1/2}G_{M-1/2} - u_{M-3/2}G_{M-3/2} + 2\nu\frac{u_M - u_{M-1}}{(l_M + l_{M-1})\,H} - 2\nu\frac{u_{M-1} - u_{M-2}}{(l_{M-1} + l_{M-2})\,H}\right) \\ \frac{1}{l_M}\left(-u_{M-1/2}G_{M-1/2} + \frac{\tau_w}{\rho} - 2\nu\frac{u_M - u_{M-1}}{(l_M + l_{M-1})\,H}\right) \end{pmatrix}.$$

Note that it is difficult to derive explicit analytical expressions for the $(M+1)$ eigenvalues of the system (9) and it is also not evident that the system (9) is hyperbolic as its associated eigenvalues may become complex. In this case, the multilayer system (9) yields to the so-called Kelvin-Helmholtz instability at the interface separating the water layers. However, an estimation of the eigenvalues in the multilayer model (9) may be used for controlling the timestep size in the numerical simulations. In this study we consider the asymptotic analysis reported in [6]. Thus, we suppose that all the velocities $(u_\alpha)_{\alpha=1,\dots,M}$ are close to the mean velocity u. A first-order approximation of the two barotropic eigenvalues yields

$$\lambda_{ext}^{\pm} = u_m \pm \sqrt{g\sum_{\alpha=1}^{M}\hbar_\alpha} + \mathcal{O}\left(|u_\beta - u|^2\right)_{\beta=1,\dots,M}, \qquad u_m = \frac{\sum_{\alpha=1}^{M}\hbar_\alpha u_\alpha}{\sum_{\alpha=1}^{M}\hbar_\alpha}, \tag{10}$$

A zeroth-order approximation of the $2(M-1)$ barotropic eigenvalues associated with $(M-1)$ interfaces gives

$$\lambda_{int}^{\pm,\alpha+\frac{1}{2}} = u \pm \sqrt{\frac{1}{2} g \sum_{\alpha=1}^{M} \hbar_\alpha} + \mathcal{O}\left(|u_\beta - u|\right)_{\beta=1,\ldots,M}, \qquad \alpha = 1,\ldots,M-1. \tag{11}$$

Notice that the eigenvalues (10)-(11) are approximations for eigenvalues of the original system using the water heights $\hbar_\alpha$ instead of the total height H. This results in a system of $2M$ equations for which each layer has two eigenvalues. It should also be stressed that for the numerical methods studied in [4], the eigenvalues associated with the single-layer counterpart of the system (1) have been used to adjust the time steps during the time integration process.

3 Runge-Kutta discontinuous Galerkin method

For the numerical solution of the multilayer shallow water system (9) we consider the Runge-Kutta scheme for the time integration and the discontinuous Galerkin (DG) method for the space discretization. Here, we divide the time interval into subintervals $[t_n, t_{n+1}]$ with length $\Delta t = t_{n+1} - t_n$ and we use the notation $\mathbf{W}^n$ to denote the value of a generic variable $\mathbf{W}$ at time t_n. To deal with the source terms $\mathbf{Q}(\mathbf{W})$ and $\mathbf{R}(\mathbf{W})$ in (9) we consider a second-order splitting method studied in [48] which consists of the following steps:

Step 1: solve for $\mathbf{W}^*$

$$\begin{aligned} \frac{\partial \mathbf{W}^*}{\partial t} &= \mathbf{R}(\mathbf{W}^*), \qquad t \in (t_n, t_{n+1/2}], \\ \mathbf{W}^*(t_n) &= \mathbf{W}(t_n). \end{aligned} \tag{12}$$

Step 2: solve for $\mathbf{W}^{**}$

$$\begin{aligned} \frac{\partial \mathbf{W}^{**}}{\partial t} + \frac{\partial \mathbf{F}(\mathbf{W}^{**})}{\partial x} &= \mathbf{Q}(\mathbf{W}^{**}), \qquad t \in (t_n, t_{n+1}], \\ \mathbf{W}^{**}(t_n) &= \mathbf{W}^*(t_{n+1/2}). \end{aligned} \tag{13}$$

Step 3: solve for $\mathbf{W}^{***}$

$$\begin{aligned} \frac{\partial \mathbf{W}^{***}}{\partial t} &= \mathbf{R}(\mathbf{W}^{***}), \qquad t \in (t_{n+1/2}, t_{n+1}], \\ \mathbf{W}^{***}(t_{n+1/2}) &= \mathbf{W}^{**}(t_{n+1}). \end{aligned} \tag{14}$$

The full time integration of the system (9) is complete once a time-stepping scheme is chosen for the solution of the three steps (12)-(14). In the current work, we consider the third-order explicit Runge-Kutta method proposed in [39] to solve the systems (12), (13) and (14). Thus, the procedure to advance the solution of an equation of the structure (12) from the time t_n to the next time t_{n+1} can be achieved by

$$\begin{aligned} \mathcal{W}^{(1)} &= \mathbf{W}^n + \Delta t \mathbf{R}(\mathbf{W}^n), \\ \mathcal{W}^{(2)} &= \frac{3}{4}\mathbf{W}^n + \frac{1}{4}\mathcal{W}^{(1)} + \frac{1}{4}\Delta t \mathbf{R}(\mathcal{W}^{(1)}), \\ \mathbf{W}^{n+1} &= \frac{1}{3}\mathbf{W}^n + \frac{2}{3}\mathcal{W}^{(2)} + \frac{2}{3}\Delta t \mathbf{R}(\mathcal{W}^{(2)}), \end{aligned} \tag{15}$$

where we have dropped the asterix of the variables for ease of notation. The formulation of the third-order explicit Runge-Kutta method for the stages (13) and (14) is carried out in the same manner as in

(15). Note that the main advantage of this scheme lies on the fact that (15) is a convex combination of the first-order Euler steps which exhibits strong stability properties. Therefore, the scheme (15) is TVD, third-order accurate in time, and stable under the standard Courant-Friedrichs-Lewy (CFL) condition. It should be stressed that the overall accuracy of the method is second-order since the splitting (12)-(14) is second-order accurate.

For the space discretization, the computational domain is partitioned into a finite set of K non-overlapping elements $\Omega_k = [x_{k-1/2}, x_{k+1/2}]$, such that

$$\Omega = \bigcup_{k=1}^{K} \Omega_k.$$

We denote by $h_k = x_{k+1/2} - x_{k-1/2}$ the length of element Ω_k in the discretized domain. As in the conventional finite element methods, the global solution is represented by a direct summation of local polynomial approximations of order $N_p - 1$ as

$$\mathbf{W}(x) \simeq \mathbf{W}_h(x) = \bigoplus_{k=1}^{K} \mathbf{W}_h^k(x),$$

and in each element Ω_k at a fixed time, the solution is locally given by a combination of N_p shape functions as

$$\mathbf{W}(\mathbf{x}^k, t) \simeq \mathbf{W}_h^k(\mathbf{x}, t) = \sum_{n=1}^{N_p} \widetilde{W}_n^k(t) \Psi_n(\mathbf{x}) = \sum_{i=1}^{N_p} W^k(x_i, t) l_i^k(\mathbf{x}), \tag{16}$$

where $\mathbf{\Psi} = \left(\Psi_1, \Psi_2, \ldots, \Psi_{N_p}\right)^T$ and $\mathbf{L} = \left(l_1, l_2, \ldots, l_{N_p}\right)^T$ are the modal and the nodal basis functions, respectively. Here, $l_i(x)$, $i = 1, \ldots, N_p$ are the Lagrange polynomials defined on the set of nodes used in combination with the chosen orthogonal basis. The basis functions Ψ_n, $n = 1, \ldots, N_p$ are selected such that $\mathbf{W}_h^k \in \mathbb{V}_k^N$, where the approximation space $\mathbb{V}_k^N$ is the set of polynomials of at most order N in each element and defined as

$$\mathbb{V}_k^N = \left\{ W : \quad W^k \in \mathscr{P}_N(\Omega_k), \ \forall \Omega_k \in \Omega \right\}. \tag{17}$$

Usually, the modal representation $\mathbf{\Psi}$ is based on the normalized Legendre polynomials $\mathscr{P}_n(\mathbf{x})$ of order n and it is reconstructed from a class of orthogonal Jacobi polynomials as

$$\Psi_n(\mathbf{x}) = \frac{\mathscr{P}_{n-1}(\mathbf{x})}{\sqrt{\gamma_{n-1}}}, \qquad \gamma_n = \frac{2}{\sqrt{2n+1}}.$$

Note that the orthonormality property of this basis set is invoked by

$$\int_{-1}^{1} \Psi_n(x) \Psi_m(x) dx = \delta_{nm},$$

with δ_{nm} denotes the Kronecker delta. In general, the nodal representation $\mathbf{L}$ is based on the Lagrange polynomials defined on the set of nodes $\{x_j\}_{j=1}^{N_p} \subset \Omega_k$ and it is used in combination with the chosen orthogonal basis $\mathbf{\Psi}$. Again, this basis satisfies the cardinal property

$$l_i^k(x_j) = \delta_{ij},$$

and the nodal degrees of freedom $W(x_j, t)$ are defined as

$$W(x_j, t) = \sum_{n=1}^{N_p} \widetilde{W}_n(t) \Psi_n(x_j), \qquad j = 1, \cdots, N_p. \tag{18}$$

From these equations (18) and by interpolating the basis functions, we establish the following relationship between the coefficients of the modal and nodal expansions

$$\mathbf{W}^k = \mathscr{V}\widetilde{\mathbf{W}}^k, \tag{19}$$

where $\widetilde{\mathbf{W}}^k = \left(\widetilde{W}_1, \widetilde{W}_2, \ldots, \widetilde{W}_{Np}\right)^T$ is the vector of the modes, $\mathbf{W}^k = \left(W(x_1), W(x_2), \ldots, W(x_{Np})\right)^T$ the vector of nodal degrees of freedom and $\mathscr{V}$ the generalized Vandermonde matrix with entries

$$\mathscr{V}_{ji} = \Psi_i(x_j), \qquad i, j = 1, \ldots, N_p.$$

A relation between the modal and nodal basis functions can also be obtained using $\mathscr{V}$ as

$$\mathbf{\Psi}\left(\mathbf{x}\right) = \mathscr{V}^T\mathbf{L}\left(\mathbf{x}\right). \tag{20}$$

It is worth remarking that the Vandermonde matrix $\mathscr{V}$ is a key for establishing the duality between modal and nodal representation provided that this matrix is nonsingular. Thus, a condition for stable and accurate simulations using the RKDG method lies on the fact that the generalized Vandermonde matrix $\mathscr{V}$ must be well-conditioned. In the current study, to guarantee this condition we use the Legendre-Gauss-Lobatto nodal points x_j. It well known that these nodes, derived from the electrostatics principle, have a good Lebesgue constant, see for example [19, 18].

In what follows we focus on the nodal representations only but the passage from the nodal to modal formulations is straightforward using the above relations. Hence, we represent the polynomial approximations of the local source term $\mathbf{Q}_h^k$ and the local flux function $\mathbf{F}_h^k$ as

$$\mathbf{Q}_h^k\left(x,t\right) = \sum_{i=1}^{N_p} \mathbf{Q}^k(x_i,t) l_i^k\left(x\right), \qquad \mathbf{F}_h^k(\mathbf{W}_h\left(x,t\right)) = \sum_{i=1}^{N_p} \mathbf{F}^k(x_i,t) l_i^k\left(x\right), \qquad \forall\, x \in [x_L^k, x_R^k]. \tag{21}$$

As in the conventional finite element methods, a weak form for the multilayer shallow water equations is obtained by multiplying (9) with Lagrange test function $l_i^k(x)$ and integrating over the local element Ω_k. Hence, using integration by parts, the weak form of the system (9) reads for $i = 1, \ldots, N_p$,

$$\int_{\Omega_k}\left(\frac{\partial \mathbf{W}_h^k}{\partial t} l_i^k - \mathbf{F}_h^k(\mathbf{W}_h^k)\frac{\partial l_i^k}{\partial x}\right) dx + \left(\widetilde{\mathbf{F}}_{k+1/2} l_i^k(x_{k+1/2}^-) - \widetilde{\mathbf{F}}_{k-1/2} l_i^k(x_{k-1/2}^+)\right) = \int_{\Omega_k} \mathbf{Q}(\mathbf{W}_h^k) l_i^k\left(x\right) dx, \tag{22}$$

where $\widetilde{\mathbf{F}}_{k+1/2} = \mathbf{F}\left(\mathbf{W}_{h,k+1/2}^-, \mathbf{W}_{h,k+1/2}^+\right)$ is a numerical flux function which allows information to be passed between the individual elements as the global approximation $\mathbf{W}_h$ may be discontinuous over internal spatial element interfaces. Here, we denote by $\mathbf{W}_{h,k+1/2}^+$ and $\mathbf{W}_{h,k+1/2}^-$ the limit values of $\mathbf{W}_h$ at $x_{k+1/2}$ from the right cell Ω_{k+1} and from the left cell Ω_k, respectively.

Note that this feature is certainly desirable for several problems with internal discontinuities such as those appearing in shock waves. In practice, the choice of the numerical flux $\widetilde{\mathbf{F}}$ can be any two-point monotone Lipschitz function that is consistent and conservative, see for instance [37]. In the current work, we consider the Lax-Friedrichs flux defined by

$$\widetilde{\mathbf{F}}\left(\mathbf{W}_h^-, \mathbf{W}_h^+\right) = \frac{1}{2}\Big(\mathbf{F}(\mathbf{W}_h^-) + \mathbf{F}(\mathbf{W}_h^+)\Big) - \frac{1}{2}\lambda\left(\mathbf{W}_h^+ - \mathbf{W}_h^-\right)\cdot\hat{\mathbf{n}}, \tag{23}$$

where $\hat{\mathbf{n}}$ is the unit normal vector on $\partial\Omega_k$ and the characteristic speed λ is calculated as

$$\lambda = \max_{1\le\alpha\le M-1}\left(\left|\lambda_{ext}^+\right|, \left|\lambda_{ext}^-\right|, \left|\lambda_{int}^{+,\alpha+\frac{1}{2}}\right|, \left|\lambda_{int}^{-,\alpha+\frac{1}{2}}\right|\right), \tag{24}$$

with $\lambda_{ext}^{\pm}$ and $\lambda_{int}^{\pm,\alpha+\frac{1}{2}}$ are the approximated eigenvalues in (10) and (11), respectively. Note that other numerical fluxes can also be used in (23) without major conceptional modifications.

3.1 Well-balanced reconstruction

The treatment of the source terms in shallow water equations presents a challenge for many numerical methods. For single layer problems, a class of well-balanced RKDG methods has been investigated in [44, 14, 36, 29] among others. Extension of these techniques to the multilayer shallow water equations (9) is not trivial. In the current study, we adapt the hydrostatic reconstruction originally developed in [5] to our RKDG method. The extension of this method to the RKDG method for the conventional shallow water equations was first proposed in [46], its application to Euler systems of gas dynamics was investigated in [28] and to blood flow problems in [27]. Hence, the source term approximation $\mathbf{Q}$ in (22) is reconstructed such that the C-property is satisfied. Recall that a numerical method is said to satisfy the well-established C-property for the equations (9) if it is compatible with quiescent steady-state solution

$$H^n + Z = C = constant, \qquad u_\alpha^n = 0, \qquad \alpha = 1, \dots, M. \tag{25}$$

To preserve this condition in our RKDG method, discretizations of the source term $\mathbf{Q}$ and the solution $\mathbf{W}$ are projected into the same space $\mathbb{V}_k^N$ using least-squares techniques. Thus, the well-balanced property is obtained by modifying the approximation (22) as

$$\int_{\Omega_k} \left(\frac{\partial \mathbf{W}_h^k}{\partial t} l_i^k - \mathbf{F}_h^k(\mathbf{W}_h^k) \frac{\partial l_i^k}{\partial x} \right) dx + \left(\widetilde{\mathbf{F}}^{\mathbf{L}}_{k+1/2} l_i^k(x_{k+1/2}^-) - \widetilde{\mathbf{F}}^{\mathbf{R}}_{k-1/2} l_i^k(x_{k-1/2}^+) \right) = \int_{\Omega_k} \mathbf{Q}(\mathbf{W}_h^k) l_i^k(x)\, dx, \tag{26}$$

Note that, compared with the standard RKDG approximation (22), we can observe that the single-valued numerical fluxes $\widetilde{\mathbf{F}}_{k+1/2}$ and $\widetilde{\mathbf{F}}_{k-1/2}$ in (26) are replaced by the left flux $\widetilde{\mathbf{F}}^{\mathbf{L}}_{k+1/2}$ and the right flux $\widetilde{\mathbf{F}}^{\mathbf{R}}_{k-1/2}$, respectively. In addition, the approximation (26) can also be reformulated as

$$\begin{aligned} \int_{\Omega_k} \left(\frac{\partial \mathbf{W}_h^k}{\partial t} l_i^k - \mathbf{F}_h^k(\mathbf{W}_h^k) \frac{\partial l_i^k}{\partial x} \right) dx + \left(\widetilde{\mathbf{F}}_{k+1/2} l_i^k(x_{k+1/2}^-) - \widetilde{\mathbf{F}}_{k-1/2} l_i^k(x_{k-1/2}^+) \right) = \\ \int_{\Omega_k} \mathbf{Q}(\mathbf{W}_h^k) l_i^k(x)\, dx + \left(\widetilde{\mathbf{F}}_{k+1/2} - \widetilde{\mathbf{F}}^{\mathbf{L}}{}_{k+1/2} \right) l_i^k(x_{k+1/2}^-) - \left(\widetilde{\mathbf{F}}_{k-1/2} - \widetilde{\mathbf{F}}^{\mathbf{R}}_{k-1/2} \right) l_i^k(x_{k-1/2}^+). \end{aligned} \tag{27}$$

Here, the left hand side of (27) is the standard DG method and the right hand side is our new approximation to the source terms. In this study, the numerical fluxes $\widetilde{\mathbf{F}}^{\mathbf{L}}_{k+\frac{1}{2}}$ and $\widetilde{\mathbf{F}}^{\mathbf{R}}_{k-\frac{1}{2}}$ in (26) are defined by

$$\widetilde{\mathbf{F}}^{\mathbf{L}}_{k+\frac{1}{2}} = \mathbf{F}\left(\mathbf{W}^{*,-}_{h,k+\frac{1}{2}}, \mathbf{W}^{*,+}_{h,k+\frac{1}{2}} \right) + \begin{pmatrix} 0 \\ \frac{g}{2}\left(H^-_{h,k+\frac{1}{2}} \right)^2 - \frac{g}{2}\left(H^{*,-}_{h,k+\frac{1}{2}} \right)^2 \\ \vdots \\ \frac{g}{2}\left(H^-_{h,k+\frac{1}{2}} \right)^2 - \frac{g}{2}\left(H^{*,-}_{h,k+\frac{1}{2}} \right)^2 \end{pmatrix}, \tag{28}$$

and

$$\widetilde{\mathbf{F}}^{\mathbf{R}}_{k-\frac{1}{2}} = \mathbf{F}\left(\mathbf{W}^{*,-}_{h,k-\frac{1}{2}}, \mathbf{W}^{*,+}_{h,k-\frac{1}{2}} \right) + \begin{pmatrix} 0 \\ \frac{g}{2}\left(H^+_{h,k-\frac{1}{2}} \right)^2 - \frac{g}{2}\left(H^{*,+}_{h,k-\frac{1}{2}} \right)^2 \\ \vdots \\ \frac{g}{2}\left(H^+_{h,k-\frac{1}{2}} \right)^2 - \frac{g}{2}\left(H^{*,+}_{h,k-\frac{1}{2}} \right)^2 \end{pmatrix}. \tag{29}$$

It should be pointed out that the reconstruction of the numerical fluxes $\widetilde{\mathbf{F}}^{\mathbf{R}}_{k-\frac{1}{2}}$ and $\widetilde{\mathbf{F}}^{\mathbf{L}}_{k+\frac{1}{2}}$ are vital for the well-balanced property and the following conditions

$$\widetilde{\mathbf{F}}^{\mathbf{L}}_{k+\frac{1}{2}} = \mathbf{F}\left(\mathbf{W}^{-}_{h,k+\frac{1}{2}}\right) \qquad \text{and} \qquad \widetilde{\mathbf{F}}^{\mathbf{R}}_{k-\frac{1}{2}} = \mathbf{F}\left(\mathbf{W}^{+}_{h,k-\frac{1}{2}}\right)$$

should be satisfied. In our reconstruction, the solutions $H^{*,+}_{h,k+\frac{1}{2}}$ and $H^{*,-}_{h,k+\frac{1}{2}}$ in (28) and (29) are approximated as

$$\begin{aligned} H^{*,+}_{h,k+\frac{1}{2}} &= \max\left(0, H^{+}_{h,k+\frac{1}{2}} - Z^{+}_{h,k+\frac{1}{2}} + \max\left(Z^{-}_{h,k+\frac{1}{2}}, Z^{+}_{h,k+\frac{1}{2}}\right)\right), \\ H^{*,-}_{h,k+\frac{1}{2}} &= \max\left(0, H^{-}_{h,k+\frac{1}{2}} - Z^{-}_{h,k+\frac{1}{2}} + \max\left(Z^{-}_{h,k+\frac{1}{2}}, Z^{+}_{h,k+\frac{1}{2}}\right)\right). \end{aligned} \tag{30}$$

Note that a similar hydrostatic reconstruction to (30) has been implemented in [5] for single-layer shallow water equations. The intermediate solutions $\mathbf{W}^{*,\pm}_{h,k+\frac{1}{2}}$ and $\mathbf{W}^{*,\pm}_{h,k-\frac{1}{2}}$ needed to evaluate the new numerical fluxes $\widetilde{\mathbf{F}}^{\mathbf{R}}_{k-\frac{1}{2}}$ and $\widetilde{\mathbf{F}}^{\mathbf{L}}_{k+\frac{1}{2}}$ are obtained using the approximations (30). Once these numerical fluxes are reconstructed, the right hand side term in (27) is computed as a volume contribution (evaluated using the projected bed elevation Z_h) and a surface contribution of the previous fluxes.

Notice that by construction the RKDG formulation (27) is local and inherently discontinuous. To rewrite (27) in a matrix form we define the elemental integrals

$$\mathcal{M}^k_{ij} = \int_{\Omega_k} l^k_i(x) l^k_j(x) dx, \qquad \mathcal{S}^k_{ij} = \int_{\Omega_k} l^k_i(x) \frac{dl^k_j(x)}{dx} dx. \tag{31}$$

Thus, the RKDG approximation (27) can be reformulated in a matrix form as

$$\begin{aligned} \mathcal{M}^k \frac{d\mathbf{W}^k_h}{dt} - \left(\mathcal{S}^k\right)^T \mathbf{F}^k_h + \left(\widetilde{\mathbf{F}}_{k+\frac{1}{2}}\delta_{N_p j} - \widetilde{\mathbf{F}}_{k-\frac{1}{2}}\delta_{1j}\right) = \\ \mathcal{M}^k \mathbf{Q}^k_h + \left(\widetilde{\mathbf{F}}_{k+\frac{1}{2}} - \widetilde{\mathbf{F}}^{\mathbf{L}}_{k+\frac{1}{2}}\right)\delta_{N_p j} - \left(\widetilde{\mathbf{F}}_{k-\frac{1}{2}} - \widetilde{\mathbf{F}}^{\mathbf{R}}_{k-\frac{1}{2}}\right)\delta_{1j}, \end{aligned} \tag{32}$$

where $\mathbf{W}^k_h = \left(\mathbf{W}^k_h(x^k_1), \mathbf{W}^k_h(x^k_2), \ldots, \mathbf{W}^k_h(x^k_{Np})\right)^T$, $\mathbf{F}^k_h = \left(\mathbf{F}^k_h(x^k_1), \mathbf{F}^k_h(x^k_2), \ldots, \mathbf{F}^k_h(x^k_{Np})\right)^T$ and $\widetilde{\mathbf{F}}$ is the vector of the associated numerical fluxes in (23). In (32), $\mathcal{M}^k$ and $\mathcal{S}^k$ are respectively, the mass and stiffness matrices the entries of which are given in (31). Here, to enable an efficient and accurate computation of the mass and the stiffness matrices in (31), we first introduce a nonsingular mapping from the reference element $\mathcal{I} = [-1, 1]$ to the kth element Ω_k as

$$\xi \longmapsto x(\xi) = x^k_L + \frac{1+\xi}{2} h_k, \qquad \xi \in \mathcal{I}.$$

We also evaluate the elemental mass and the stiffness matrices (31) in terms of the computational variables ξ as

$$\mathcal{M}^k_{ij} = \frac{h_k}{2}\int_{-1}^{1} l_i(\xi) l_j(\xi) d\xi = \frac{h_k}{2}\mathcal{M}_{ij}, \qquad \mathcal{S}^k_{ij} = \int_{-1}^{1} l_i(\xi)\frac{dl_j(\xi)}{d\xi} d\xi = \mathcal{S}_{ij},$$

with $\mathcal{M}$ and $\mathcal{S}$ are the equivalent standard mass and stiffness matrices, respectively. Note that using the explicit expressions of derivatives of the basis functions Ψ_j and the duality between nodal and modal representations, the computation of these matrices can be carried out in a straightforward manner, see for example [21, 17]. Thus, the semi-discrete formulation (32) becomes

$$\frac{h_k}{2}\mathcal{M}\frac{d\mathbf{W}^k_h}{dt} - \left(\mathcal{S}^k\right)^T \mathbf{F}^k_h = \frac{h_k}{2}\mathcal{M}\mathbf{Q}^k_h + \left(\widetilde{\mathbf{F}}^{\mathbf{R}}_{k-\frac{1}{2}}\delta_{1j} - \widetilde{\mathbf{F}}^{\mathbf{L}}_{k+\frac{1}{2}}\delta_{N_p j}\right), \tag{33}$$

which can be reformulated as a system of ordinary differential equations for the following compact form

$$\begin{aligned} \frac{d\mathbf{W}}{dt} &= \mathcal{H}(\mathbf{W}), \\ \mathbf{W}(0) &= \mathbf{W}_0, \end{aligned} \tag{34}$$

where $\mathcal{H}$ is the spatial discretization in (33) and $\mathbf{W}_0$ is a given initial data, compare [21, 20] for a similar detailed derivation of (34).

The time integration of the equations (34) is carried out using the explicit third-order Runge-Kutta scheme. The implementation of this method is performed using the same steps as in (15) and for brevity will not be repeated here. In the current work, to eliminate non-physical oscillations and to obtain high-order stability for the high space discretization $k \geq 1$, a slope limiter procedure is performed after each inner stage in the Runge-Kutta time stepping. There exist several choices for the slope limiters to be implemented for the RKDG method, see for instance [22, 49] for an overview. In our simulations, we use the Total Variation Diminishing (TVD) limiter studied in [9, 23, 39, 41] among others. Note that other slope limiter functions can also be applied in our RKDG method without major conceptional modifications.

4 Numerical examples

Numerical results for several test examples of multilayer free-surface flows are presented in this section. We examine the performance of our well-balanced RKDG method for dam-break flow problems and wind-driven recirculation flows in both flat and non-flat beds. We also present numerical comparisons to the well-established kinetic method studied in [35] and a finite volume (FV) method proposed in [4]. The results obtained using the RKDG method for a dam-break problem are also compared to those obtained using the three-dimensional model for free-surface flows. Here, the three-dimensional hydrostatic incompressible Navier-Stokes equations are solved using the TELEMAC-3D software*. In our simulations, the total water height H and the total number of layers M are given whereas, the water height $\hbar_\alpha$ at each αth layer is equidistantly calculated as

$$\hbar_\alpha = l_\alpha H, \qquad \text{with} \qquad l_\alpha = \frac{1}{M}, \qquad \alpha = 1, 2, \ldots, M.$$

In addition, the courant number is set to $Cr = 0.85$ in all the examples and the time stepsize Δt is adjusted at each step according to the CFL condition

$$\Delta t = Cr \min_{1\leq k\leq K} \left(\frac{h_k}{\max\limits_{1\leq\alpha\leq M-1} \left(\left|\lambda^+_{ext}\right|, \left|\lambda^-_{ext}\right|, \left|\lambda^{+,\alpha+\frac{1}{2}}_{int}\right|, \left|\lambda^{-,\alpha+\frac{1}{2}}_{int}\right| \right)} \right),$$

where $\lambda^{\pm}_{ext}$ and $\lambda^{\pm,\alpha+\frac{1}{2}}_{int}$ are the approximated eigenvalues in (10) and (11), respectively. For a better insight in the results we also generate the two-dimensional velocity fields from our RKDG results using the post-processing procedure described in [6]. Thus, the vertical velocity v is computed using the divergence-free condition from the incompressible Navier-Stokes equations as

$$\frac{\partial u}{\partial x} + \frac{\partial v}{\partial z} = 0. \tag{35}$$

To obtain the vertical velocity v, the equation (35) is integrated for each layer assuming non-penetration boundary conditions at the bottom. We refer to [6] for more details on the computation of vertical velocity for multilayer shallow water equations.

*See http://www.opentelemac.org for more details on the TELEMAC-3D software.

4.1 Accuracy problems

We present numerical results for a class of test examples to investigate the accuracy of the proposed RKDG method for solving the multilayer shallow water equations. We first examine the performance of the RKDG method using different degrees of the polynomial approximation and different numbers of gridpoints. To this end we consider the frictionless two-layer version of the problem (1) reformulated as

$$\begin{aligned}
\frac{\partial H}{\partial t}+\frac{\partial \hbar_1 u_1}{\partial x}+\frac{\partial \hbar_2 u_2}{\partial x} &= 0,\\
\frac{\partial \hbar_1 u_1}{\partial t}+\frac{\partial}{\partial x}\left(\hbar_1 u_1^2+g\hbar_1^2\right) &= -g\hbar_1\frac{\partial Z}{\partial x}+u_{3/2}G_{3/2}+2\nu\frac{u_2-u_1}{\hbar_1+\hbar_2},\\
\frac{\partial \hbar_2 u_2}{\partial t}+\frac{\partial}{\partial x}\left(\hbar_2 u_2^2+g\hbar_2^2\right) &= -g\hbar_2\frac{\partial Z}{\partial x}-u_{3/2}G_{3/2}-2\nu\frac{u_2-u_1}{\hbar_1+\hbar_2},
\end{aligned} \tag{36}$$

where $\hbar_1=\hbar_2=\frac{1}{2}H$, $G_{3/2}=\frac{1}{2}\left(\frac{\partial \hbar_1 u_1}{\partial x}-\frac{\partial \hbar_2 u_2}{\partial x}\right)$ and

$$u_{3/2}=\begin{cases} u_1, & \text{if} \quad G_{3/2}\geq 0,\\ \\ u_2, & \text{if} \quad G_{3/2}<0. \end{cases}$$

Here, we solve the equations (36) in the spatial domain $[0,1]$ on a non-flat bottom defined as

$$Z(x)=\sin^2(\pi x),$$

and subject to the following initial conditions

$$H(x,0)=5+e^{\cos(2\pi x)}-Z(x), \qquad u_1(x,0)=u_2(x,0)=0.$$

The viscosity coefficient $\nu=0.001\ m^2/s$, the gravity $g=9.81\ m/s^2$ and periodic boundary conditions are used. Note that a similar test example has been presented in [45] for the standard single-layer shallow water equations. In order to quantify the errors in this example, a reference solution computed using a fine mesh of 16000 gridpoints and a degree of polynomial approximation $N=5$ is used as an exact solution. We compute the numerical solutions at time $t=0.15$ using different numbers of gridpoints K and approximation orders N. We consider the relative L^1-error defined as

$$L^1\text{-error}=\frac{\displaystyle\sum_{k=1}^{K}\left|\mathcal{U}_k^n-\mathbf{U}^k(x_k,t)\right|\Delta x}{\displaystyle\sum_{k=1}^{K}\left|\mathbf{U}^k(x_k,t)\right|\Delta x}, \tag{37}$$

where $\mathcal{U}_k^n$ and $\mathbf{U}^k(x_k,t)$ are respectively, the computed and exact solutions at gridpoint x_k and time t, whereas K stands for the number of gridpoints used in the spatial discretization. The obtained results for the total water height H and the interface velocity u_1 are summarized in Table 1 using different values of N and K. It is evident that increasing the degree of the polynomial approximation or the number of gridpoints in the computational domain, the errors are relatively small, however the errors in the water height H are consistently lower than the errors in the velocity u_1. For the considered flow conditions in this test example, we observe that nearly the optimal convergence rates are achieved in our RKDG method using the L^1-error norm for both solutions H and u_1. Similar results, not reported here for brevity, have been observed in the errors obtained for the velocity u_2. It is worth pointing out that the method with P^k elements should give a uniform $(k+1)$th order of accuracy however, we only observe convergence rates of kth order in Table 1. This may be attributed to the fact that these convergence rates

Table 1: Errors for the accuracy test problem using different numbers of gridpoints and approximation orders in the RKDG method.

	Errors in H									
K	$N=1$	Rate	$N=2$	Rate	$N=3$	Rate	$N=4$	Rate	$N=5$	Rate
50	2.65945E-01	—	1.62427E-01	—	1.07812E-01	—	8.5713E-02	—	6.8870E-02	—
100	1.35296E-01	0.98	4.13451E-02	1.97	1.37310E-02	2.97	5.4620E-03	3.97	2.1958E-03	4.97
200	6.83076E-02	0.99	1.04443E-02	1.99	1.73551E-03	2.98	3.4542E-04	3.98	6.9480E-05	4.98
400	3.42248E-02	1.00	2.61832E-03	2.00	2.17691E-04	3.00	2.1678E-05	3.99	2.1818E-06	4.99
800	1.69002E-02	1.02	6.48258E-04	2.01	2.69112E-05	3.02	1.3408E-06	4.02	6.7522E-08	5.01

	Errors in u_1									
K	$N=1$	Rate	$N=2$	Rate	$N=3$	Rate	$N=4$	Rate	$N=5$	Rate
50	3.93517E-01	—	1.88545E-01	—	1.34092E-01	—	1.00796E-01	—	8.1081E-02	—
100	2.00892E-01	0.97	4.81266E-02	1.97	1.71136E-02	2.97	6.42321E-03	3.97	2.5870E-03	4.97
200	1.01848E-01	0.98	1.21996E-02	1.98	2.16906E-03	2.98	4.06209E-04	3.98	8.1972E-05	4.98
400	5.12782E-02	0.99	3.07111E-03	1.99	2.73018E-04	2.99	2.54938E-05	3.99	2.5794E-06	4.99
800	2.54619E-02	1.01	7.62474E-04	2.01	3.38915E-05	3.01	1.57688E-06	4.02	8.0049E-08	5.01

are computed using a reference solution and not the genuine analytical solution of the problem. Thus, the numerical errors inherited in this reference solution may lead to a deterioration in the convergence rates of the method.

To examine the well-balanced property of the proposed RKDG method for multilayer shallow water flows, we consider the problem of a lake at rest flow studied in [4]. This test example has been first proposed in [7] to test the conservation property of numerical methods for the conventional single-layer shallow water equations over non-flat beds. The lake bed is irregular and it is a good illustration of the significance of the numerical treatment for the source terms for practical applications to natural watercourses. Here, it is expected that the total water free-surface remains constant and the water velocity should be zero at all times. As in [7, 4], we consider a mesh with 100 gridpoints and the obtained results are displayed at time $t = 10800\ s$ with the degree of the polynomial approximation set to $N = 3$. The obtained numerical results for the water interfaces and the water free-surface along with the considered lake bed are displayed in Figure 2. We present results obtained using the 10-layer and 20-layer models and for comparison reasons, the errors in the difference between the exact and the computed total water free-surface using 5-layer, 10-layer and 20-layer models are also exhibited in Figure 3. It is clear from the results shown in both Figure 2 and Figure 3 that the water free-surface remains constant during the simulation times and the proposed RKDG method preserves the C-property to the machine precision. It should be noted that the performance of the proposed RKDG method is very interesting as the obtained solutions satisfy the conservation property even when coarse meshes are used without requiring complicated discretizations to balance the source terms and flux gradients in the multilayer shallow water equations.

4.2 Dam-break problem on a flat bottom

We consider a dam-break problem over a flat bottom in the computational domain $[-50, 50]$ equipped with the following initial conditions

$$H(x,0) = \begin{cases} 2, & \text{if} \quad x \leq 0, \\ \\ 1, & \text{if} \quad x > 0, \end{cases} \qquad u_\alpha(x,0) = 0.$$

This example has been solved in [6] using the kinetic scheme and in [4] using a class of finite volume methods. Therefore, we use the same dimensionless viscosity coefficient $\nu = 0.01$, the gravity $g = 2$

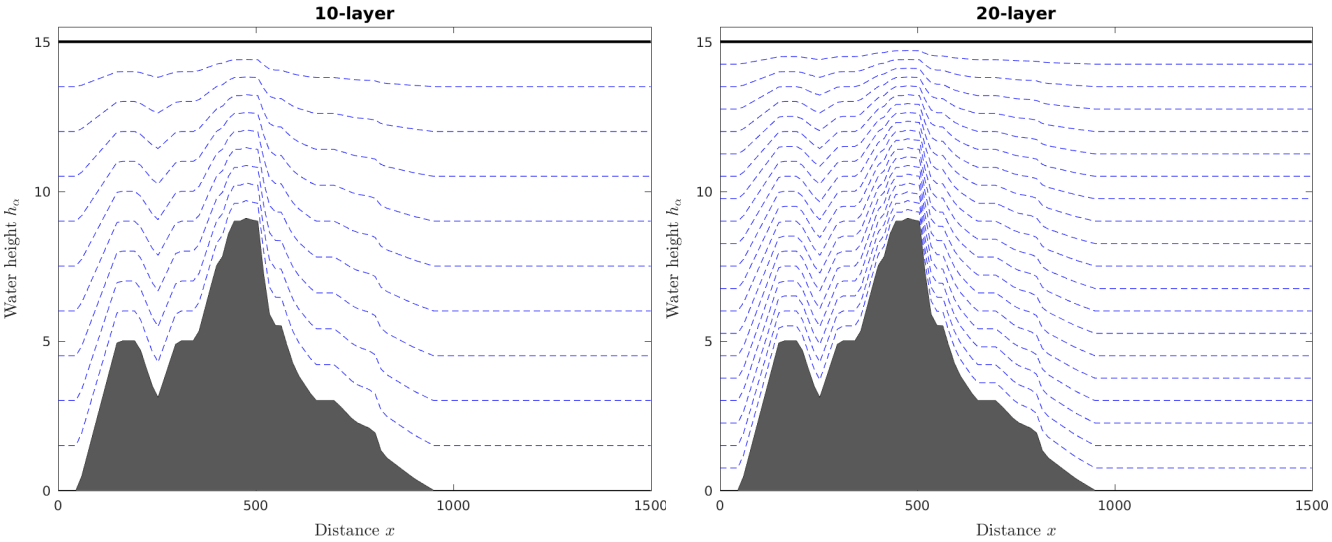

Figure 2: Results obtained for water interfaces (dashed blue lines) and water free-surface (solid black line) for the lake at rest flow at time $t = 10800$ s using 10-layer model (left plot) and 20-layer model (right plot).

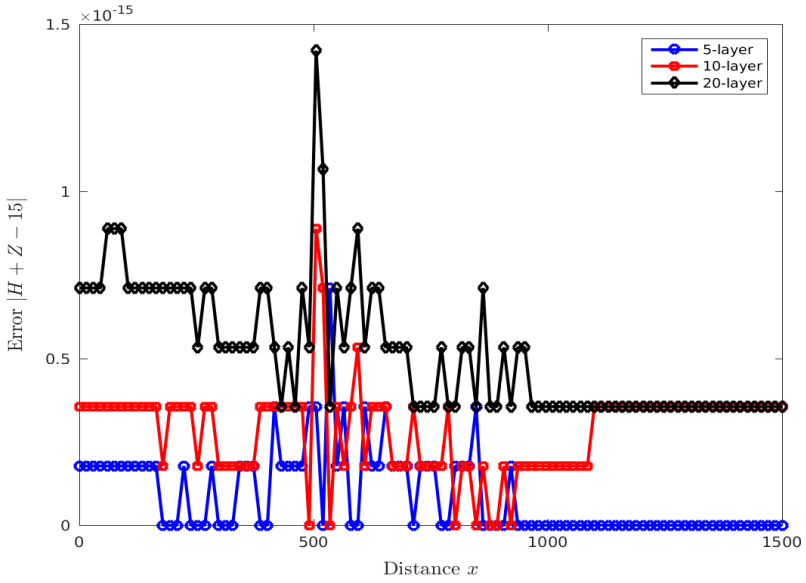

Figure 3: Differences between the exact and the computed total water free-surface for the lake at rest flow at time $t = 10800$ s using 5-layer, 10-layer and 20-layer models.

and the friction coefficient $\kappa = 0.1$ as in [6, 4]. The computational domain is discretized in 100 and 200 elements, the degree of the polynomial approximation is set to $N = 3$, and numerical results are presented at time $t = 14$.

In Figure 4 we display the water heights obtained using our RKDG method compared to the kinetic and FV methods using 10 layers on the considered meshes. For comparison reasons we have also included with these results a reference solution obtained on a fine mesh with 10000 elements using the kinetic method. As expected for most dam-break problems, the flow structure consists of a shock wave traveling downstream and a rarefaction wave traveling upstream in the computational domain. As it can be seen from the results presented in Figure 4, the solutions obtained using the kinetic and FV methods

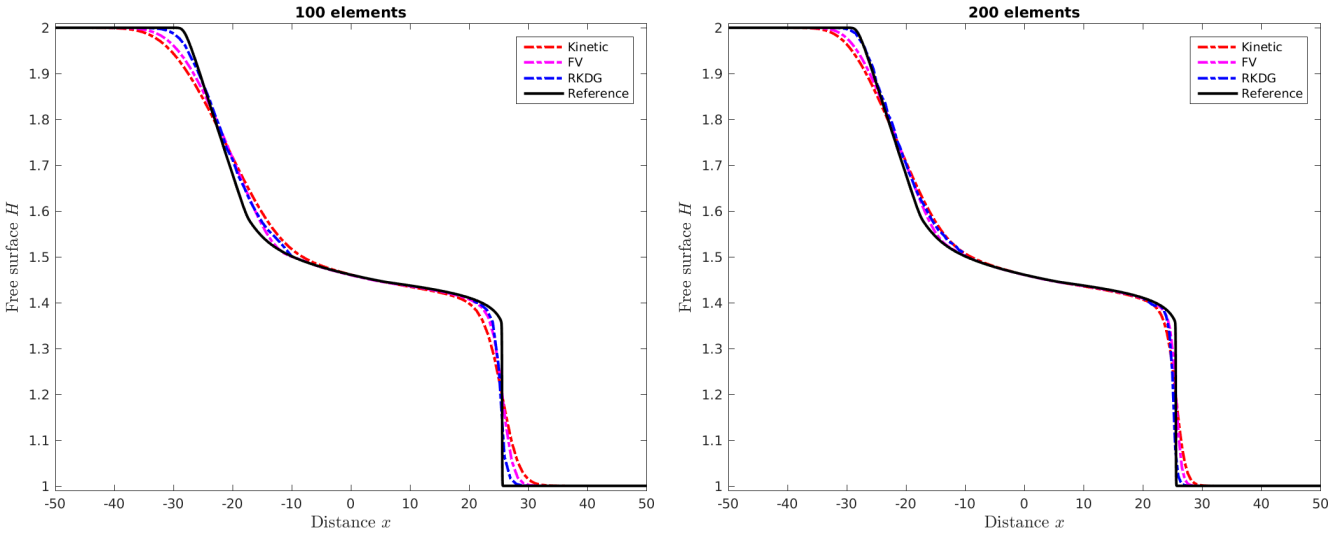

Figure 4: Free-surface results for 10-layer model at time $t = 14$ obtained using 100 elements (left plot) and 200 elements (right plot) for the dam-break on a flat bottom.

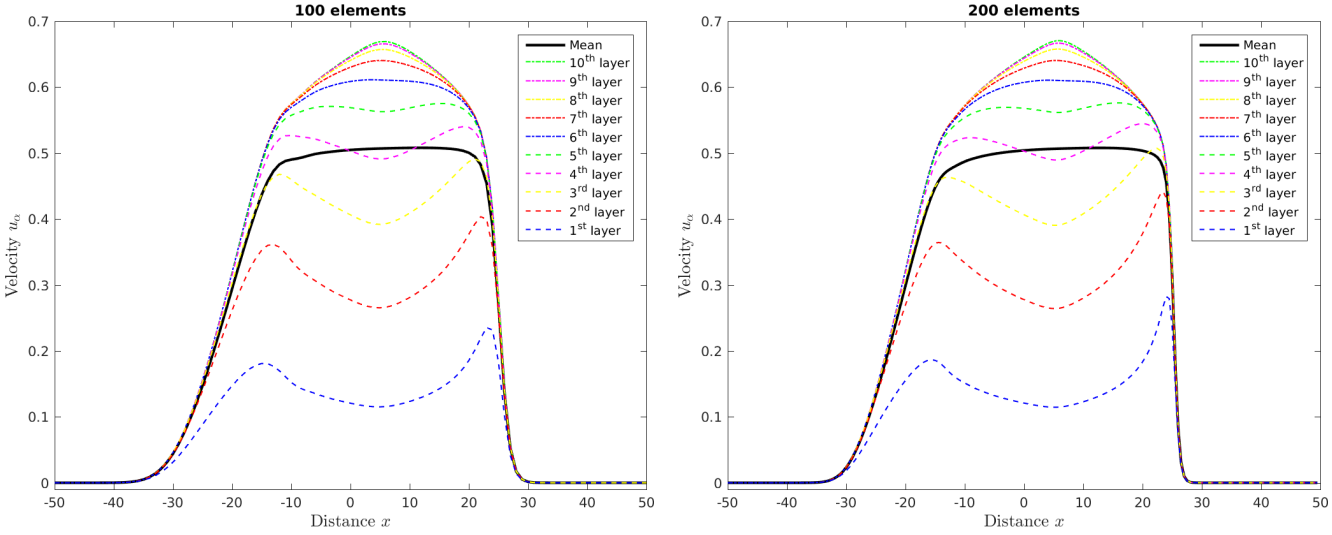

Figure 5: Velocity results for the 10-layer model at time $t = 14$ obtained using 100 elements (left plot) and 200 elements (right plot) for the dam-break on a flat bottom. Dashed lines refer to the velocity at the interfaces and solid lines to the mean velocity.

on the coarse mesh with 100 elements are more diffusive than the RKDG solutions. Obviously, this numerical diffusion is reduced by refining the mesh from 100 to 200 elements but still the RKDG method produces the most accurate results followed by the FV method. The same accuracy has been observed for comparisons not included here, for 20 layers in the model. It is evident that the proposed RKDG method performs well for this dam-break flow problem and it correctly captures the rarefaction wave and the shock without need for very fine meshes in the simulations. In Figure 5 we illustrate the velocity at the water interfaces between the layers obtained using 10 layers on the considered meshes with 100 and 200 elements. The mean velocity is also depicted along the water velocities in these figures. It is clear from the velocity profiles presented in Figure 5 that the RKDG method accurately resolves this test example and it produces numerical results similar to those obtained using the FV method in [4]. Therefore, the performance of our RKDG method is very attractive since the computed solutions remain

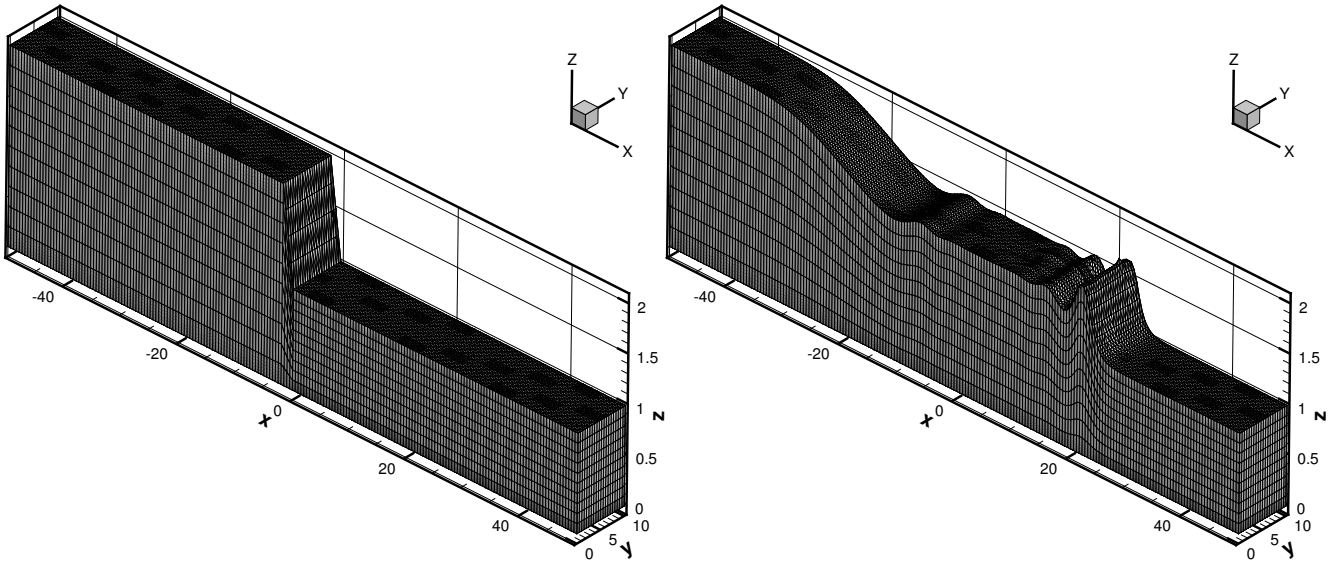

Figure 6: Water free-surface at time $t = 0$ (left plot) at time $t = 14$ (right plot) for the three-dimensional simulation of dam-break on a flat bottom.

stable and highly accurate without requiring solvers for Riemann problems or linear systems of algebraic equations in the hyperbolic parts.

Next we compare the results obtained using the multilayer shallow water model to those obtained using the TELEMAC-3D model and the three-dimensional incompressible Navier-Stokes equations for this test example. In Figure 6 we present the initial water free-surface and the result obtained at time $t = 14$ for the three-dimensional simulations. Here, a mesh with 9840 elements and 5907 nodes is used in the three-dimensional computations along with a fixed time step $\Delta t = 0.01$. A comparison between the cross-section of the TELEMAC-3D results at $y = 5$ and those obtained using the RKDG method with 200 elements for 10-layer model is depicted in Figure 7. It is clear from these results that the location and the speed of the moving water front obtained using the multilayer model agree well to those computed using the TELEMAC-3D model. Note that fluctuations with different amplitudes appear in the TELEMAC-3D results which are completely absent in the results obtained using the multilayer model. These fluctuations are mainly cause by the turbulent effects accounted for in the TELEMAC-3D model and are also in good agreement with the experimental data reported in [34] for this class of dam-break flows.

In Figure 8 we present the velocity profiles at the location $x = 8$ obtained using these models at time $t = 14$. Here, we consider 5-layer, 10-layer and 20-layer in our simulations using the mesh with 200 elements. It is clear that the flow velocity varies within the water depth which is not the case in the standard single-layer shallow water equations widely used in the literature to model dam-break problems. For example, at the location $x = 8$ in the computational domain, the water velocity at the surface is more than six times higher than the water velocity at the bottom. As can be seen from Figure 8, an increase of the number of layers in the one-dimensional multilayer model yields a consistent convergence to the velocity profile obtained using the three-dimensional incompressible Navier-Stokes equations. These results are a clear indication that it is possible to efficiently resolve the vertical variation in the water velocity using one-dimensional multilayer shallow water equations without need to the three-dimensional incompressible Navier-Stokes equations with moving boundary conditions. Indeed, for the considered dam-break conditions, the RKDG method generates numerical results as accurate as those simulated using the three-dimensional incompressible Navier-Stokes equations subject to free-surface conditions but with a very low computational cost as only a set of one-dimensional multilayer equations are considered. As pointed out before, the discrepancy between the results obtained using the TELEMAC-3D model and those obtained using the RKDG method in Figure 8 is due to the turbulent effects accounted for in the

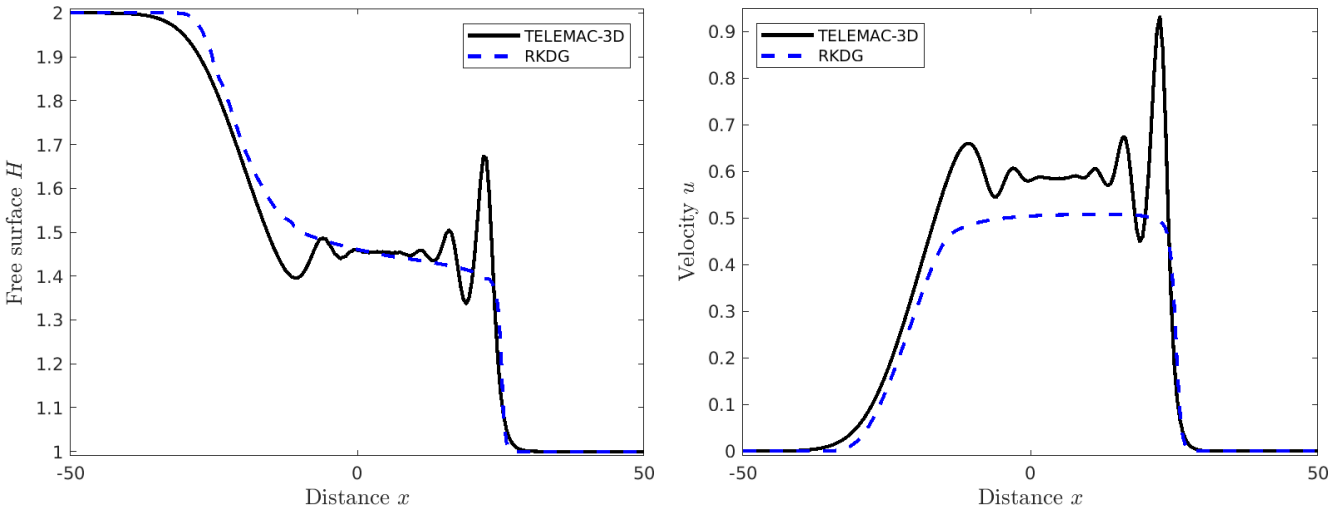

Figure 7: Comparison between TELEMAC-3D and RKDG results obtained for the water free-surface (left plot) and velocity (right plot) using 10-layer model at time $t = 14$ for the dam-break on a flat bottom.

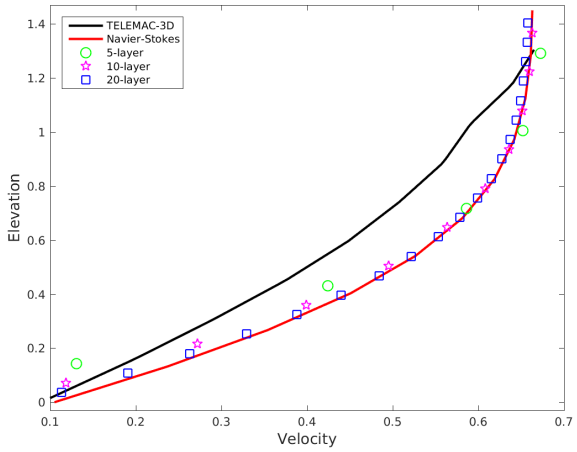

Figure 8: Profiles of the velocity at $x = 8$ obtained using a mesh with 100 elements at time $t = 14$ for the dam-break on a flat bottom.

model for dam-break problems using the TELEMAC-3D software.

4.3 Wind-driven recirculation flow on a flat bottom

In this example we consider a class of wind-driven recirculation problems in closed flow domains studied in [38, 4] among others. It is necessary to point out that this recirculation features of the water flow can not be captured using the conventional single-layer shallow water equations. Hence, the present test example is served as a prototype to verify the performance of multilayer shallow water flows to reproduce such phenomena, see for instance [6, 42, 4]. Here, the multilayer system (1) is solved in a closed lake 16 m long with flat bottom topography and filled at 2 m. The water flow enters the lake from the left boundary with a speed of $w = 20$ m/s and it flows towards the right exit of the lake. At later time, due to the wind effects, the water flow changes the direction pointing towards the right coast of the

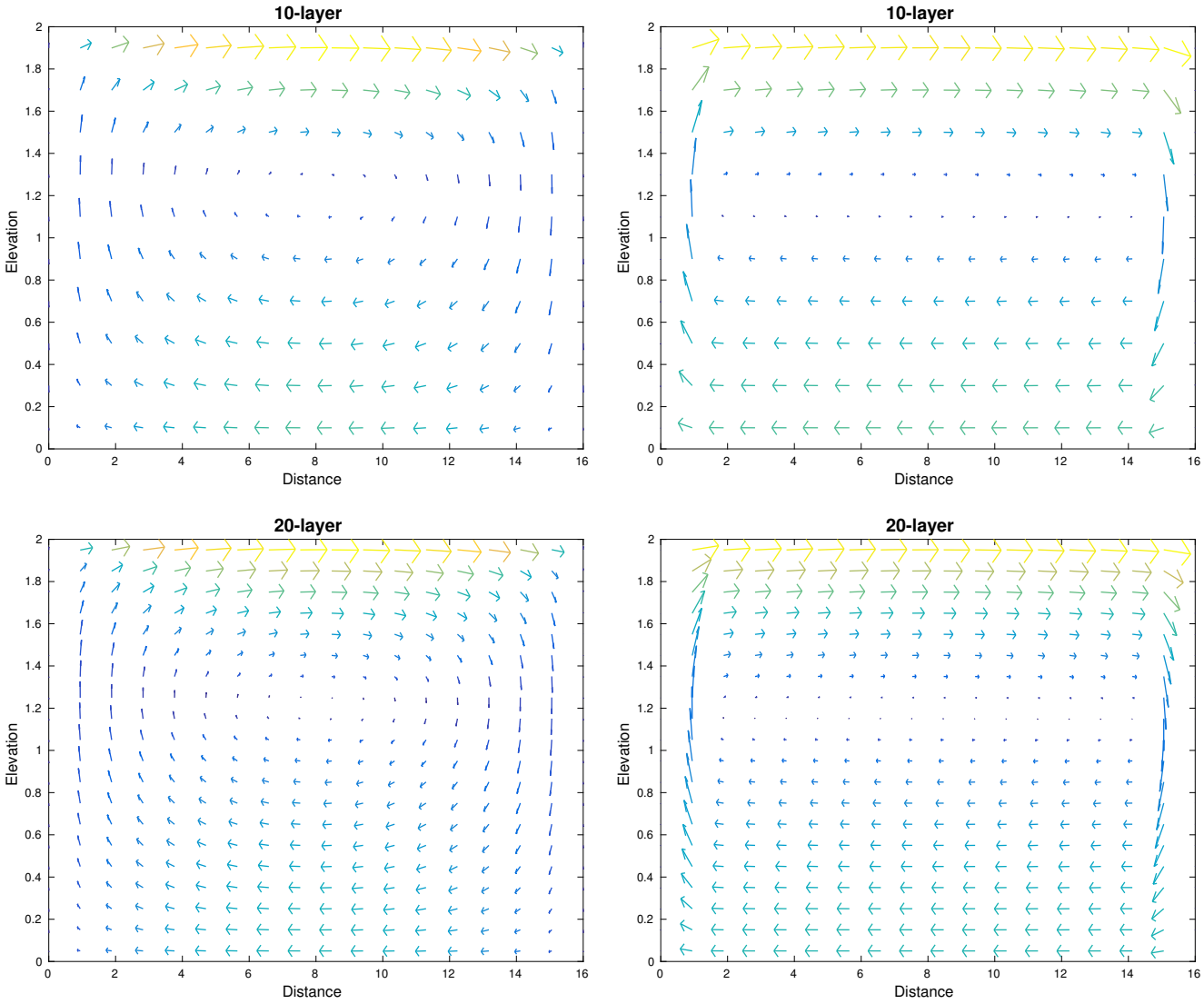

Figure 9: Velocity fields obtained for the recirculation flow on a flat bottom with 10-layer model (first row) and 20-layer model (second row) using the kinetic method (left column) and the RKDG method (right column) on a mesh of 16 elements at time $t = 20\ s$. Colors represent the magnitude of the velocity.

lake. The flow parameters are those used in [4] including, viscosity coefficient $\nu = 0.1\ m^2/s$, friction coefficient $\kappa = 0.00001\ m/s$, wind stress coefficient $\sigma_s^2 = 0.0015$, water density $\rho = 1000\ kg/m^3$, air density $\rho_a = 1.2\ kg/m^3$ and gravity $g = 9.81\ m/s^2$. The computations are performed for this example using 16 elements and a degree of polynomial approximation $N = 3$.

Figure 9 exhibits the velocity fields obtained at time $t = 20\ s$ for 10-layer and 20-layer models using the kinetic and RKDG methods on a mesh of 16 elements. As can be seen, a central recirculation has been generated in the flow domain and the center of this vortex is clearly affected by the number of layers used in the computations. It is also clear that the RKDG results are more accurate than those obtained using the kinetic method. Note the excessive numerical diffusion in the results obtained using the kinetic method in Figure 9. For the considered flow conditions, the kinetic method fails to accurately resolve the wall effects on the velocity fields whereas those effects are well captured by the RKDG method. As in the previous test example, we also display in Figure 10 the velocity profiles at the location $x = 6\ m$ obtained using different numbers of layers at time $t = 20\ s$. Here, we consider the 5-layer, 10-layer, 20-layer and 30-layer models using the mesh with 16 elements. For comparison reasons, we also include a reference

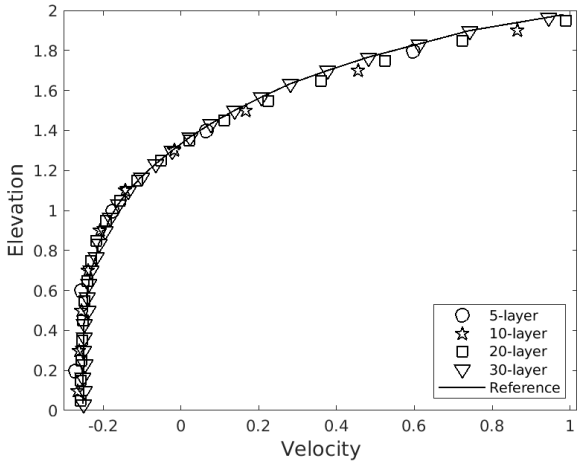

Figure 10: Velocity profiles at $x = 6\ m$ obtained at time $t = 20\ s$ for the recirculation flow on a flat bottom using different numbers of layers.

solution for the velocity obtained using 50-layer model and a very fine mesh of 16000 elements. It is clear that an increase of number of layers in the model results in a perfect convergence to the reference solution. For this example, the differences between results for the vertical velocity depicted in Figure 10 using 10-layer, 20-layer and 30-layer models are minimal. In addition, the presented results for this wind-driven recirculation flow problem demonstrate the ability of our RKDG method to capture the small flow features within the channel without generating spurious oscillations. For example, a simple inspection of these results shows that the wall flow pattern is accurately resolved by the proposed well-balanced RKDG method.

4.4 Transcritical flow over a bump

We turn our attention to test examples for multilayer shallow water flows over non-flat beds. We first consider the example of a flow over a frictionless parabolic bump investigated in [13]. Hence, the bed is given as

$$Z(x) = \max\left(0, 0.2 - 0.05\,(x-10)^2\right),$$

and at initial time, the system is at rest with the total water height given by

$$H(x,t) = 0.33\ m - Z(x).$$

As in [13], the computational domain is 20 m long, the kinematic viscosity $\nu = 0.0001\ m^2/s$ and the gravity constant $g = 9.81\ m/s^2$. For the boundary conditions, we consider an upstream boundary condition on the water discharge $Hu_\alpha = 0.36^{\frac{\alpha-1}{M}}\ m^2/s$ and a downstream boundary condition on the water level equal to $H = 0.33\ m$. In our simulations, the degree of the polynomial approximation $N = 6$ and steady-state solutions are presented.

A mesh convergence study is also performed for this test example to assess the accuracy of the proposed RKDG method. The obtained results for the water height at the interfaces using 50, 100, 200 and 400 elements are depicted in Figure 11. We present results obtained for 10-layer and 20-layer models and we also include a zoom in the results for a better comparison. As expected, the flow reaches the stationary regime and yields a transition between subcritical and supercritical flow conditions forming an hydraulic jump over the bump. Under the considered flow conditions, the effects of mesh refinements on the free-surface seems to be minimal outside the region of the hydraulic jump. However, these effects become

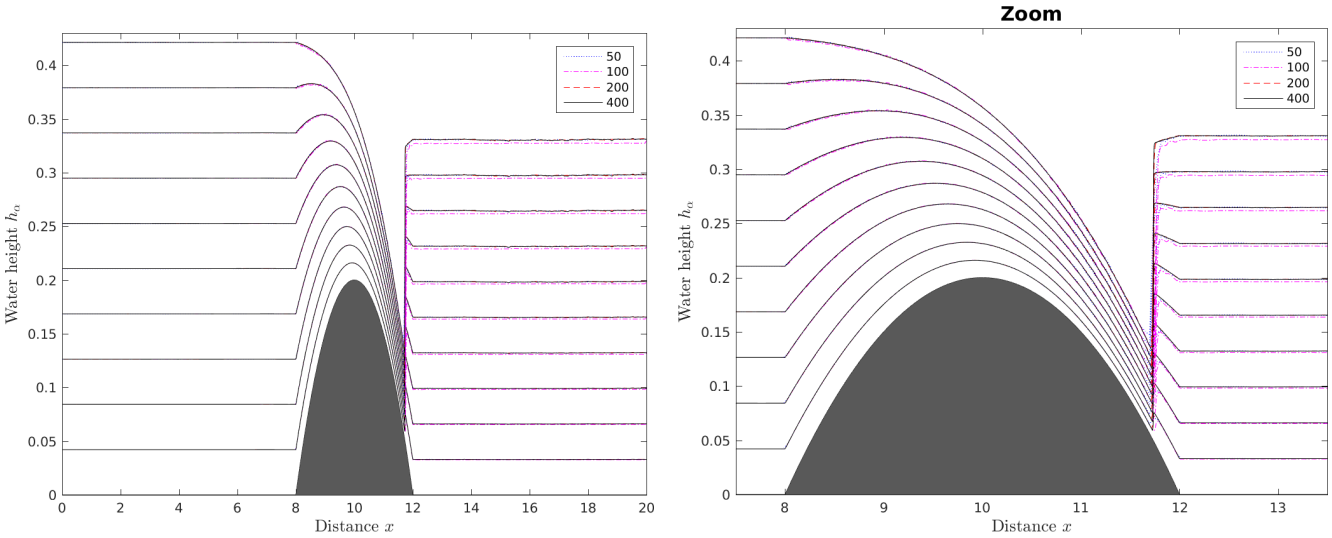

Figure 11: Free-surface profiles obtained for the transcritical flow over a bump using 10-layer model and different meshes at the steady state.

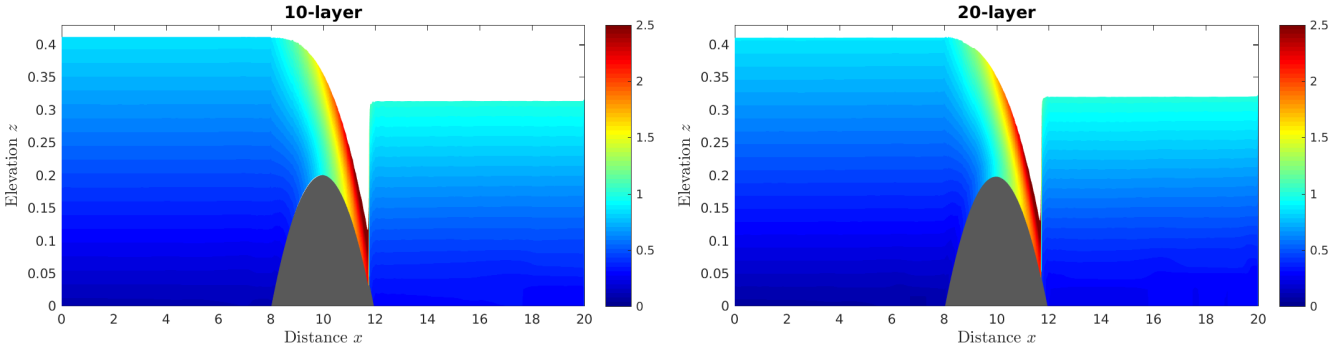

Figure 12: Distribution of the velocity intensity for the transcritical flow over a bump using 10-layer model (left plot) and 20-layer model (right plot) at the steady state.

more pronounced at the shock regions and more accurate results are obtained for fine meshes, compare the zoom plot in Figure 11. This ensures grid convergence of the numerical results using the RKDG method. For this test example, increasing the number of elements in the simulations results in a small difference in the results but at high computational cost. Here, increasing the number of elements from 200 to 400 results in an increase in the CPU time of more than 3.5 times. Therefore, bearing in mind the slight change in the results from the mesh with 200 elements and the mesh with 400 elements at the expense of rather significant increase in the computation time, the mesh with 200 elements is believed to be adequate to obtain computational results free of grid effects for the considered multilayer shallow water problem of transcritical flow over a bump.

In Figure 12 we present the distribution of velocity intensities for 10-layer and 20-layer models using the mesh of 200 elements. High velocity intensities are detected when the water flows over the bump with a noticeable difference in these intensities between the 10-layer and 20-layer models. It is also clear that a sharper hydraulic jump is obtained in the results obtained using the 20-layer model than those obtained using the 10-layer model. The proposed RKDG method resolves the correct dynamics for this multilayer flow problem and converges to the expected steady-state solution. As can be seen, there is no numerical instability or smearing in the computed solution at the hydraulic jump as those visible in the results reported in [13]. The proposed RKDG method accurately resolves this multilayer flow over a bump

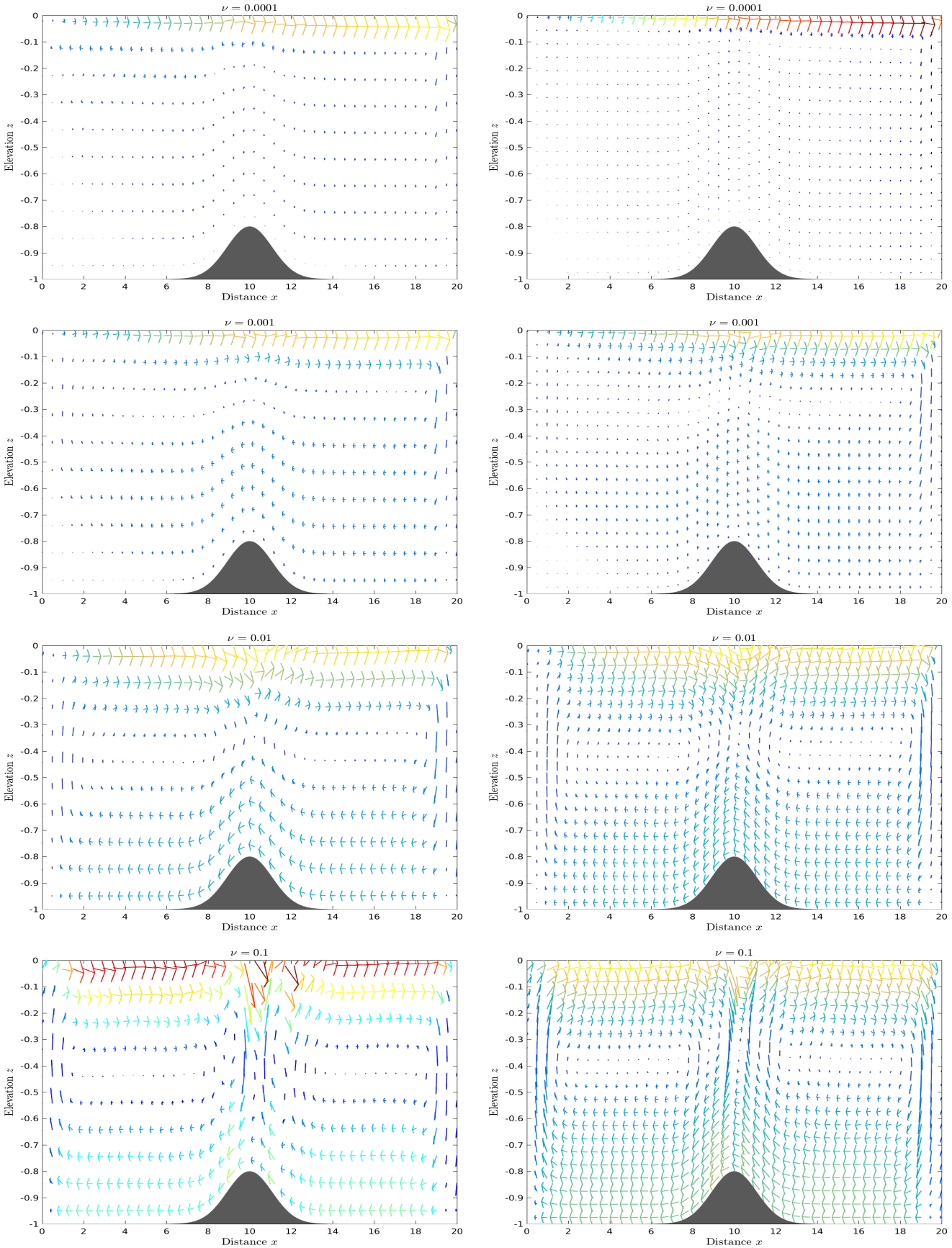

Figure 13: Velocity fields obtained for the wind-driven recirculation flow problem at time $t = 50\ s$ using 10-layer model (first column) and 20-layer model (second column) and different values of the viscosity.

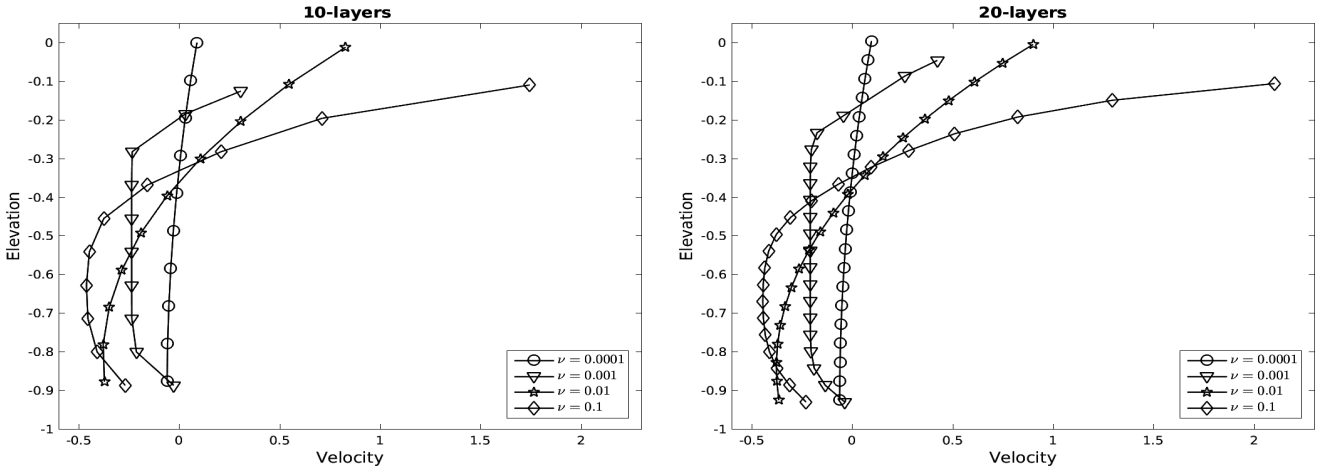

Figure 14: Velocity profiles at $x = 12.2\ m$ obtained for the wind-driven recirculation flow problem at time $t = 50\ s$ using 10-layer model (left plot) and 20-layer model (right plot) and different values of the viscosity.

without exhibiting nonphysical oscillations. The results obtained for this test example also demonstrate that our well-balanced RKDG method performs very satisfactorily for this multilayer shallow water flow problem since it does not produce excessive numerical dissipation in the moving fronts and no spurious oscillations have been detected near the hydraulic jump over the bump in the computational domain.

4.5 Wind-driven recirculation flow over a hump

This test example consists of a wind-driven recirculation flow over a hump using the multilayer shallow water equations. The objectives of this flow problem are to examine the ability of the proposed RKDG method to recover recirculation flows over non-flat beds and also to assess the effects of viscous terms on the multilayer system. Here, we solve the equations (1) in a channel 20 m long with a non-flat bed defined as

$$Z(x) = 0.2 \exp\left(-0.42(x-10)^2\right).$$

We assume an uniform wind stress of $\sigma = 1.5\ N/m^2$ applied at the surface which is equivalent to a wind speed of $w = 20\ m/s$ blowing from the left of the channel. Initially, the system is at rest with the total water height given by

$$H(0,x) = 1\ m - Z(x).$$

The computational domain is discretized into 40 elements, the degree of the polynomial approximation is fixed to $N = 3$ and the computed water velocity fields are illustrated in Figure 13 at time $t = 50\ s$ using 10 and 20 layers. We present results obtained using four different values of the viscosity coefficients namely, $\nu = 0.0001$, 0.001, 0.01 and 0.1. It is clear from the presented results that the RKDG method performs well for this multilayer problem over non-flat topography and it captures the expected water dynamics. For instance, no spurious oscillations are detected on the water free-surface or near the bed without need for very fine meshes in the computational domain or high polynomial degrees in the RKDG method. On the other hand, increasing the number of layers in the system from 10 to 20 layers results in a smooth and fully symmetric velocity field for all selected values of the viscosity coefficient ν.

The effects of the viscosity coefficient ν in the computational results for this test example can also be seen in Figure 13. Note that from the definition of the vertical kinematic eddy viscosity (6), the coefficient ν allows for the exchange between the layers in the system (1). In Figure 14 we present the velocity profiles in a point situated behind the hump at $x = 12.2\ m$ using 10 and 20 layers for the considered values of the

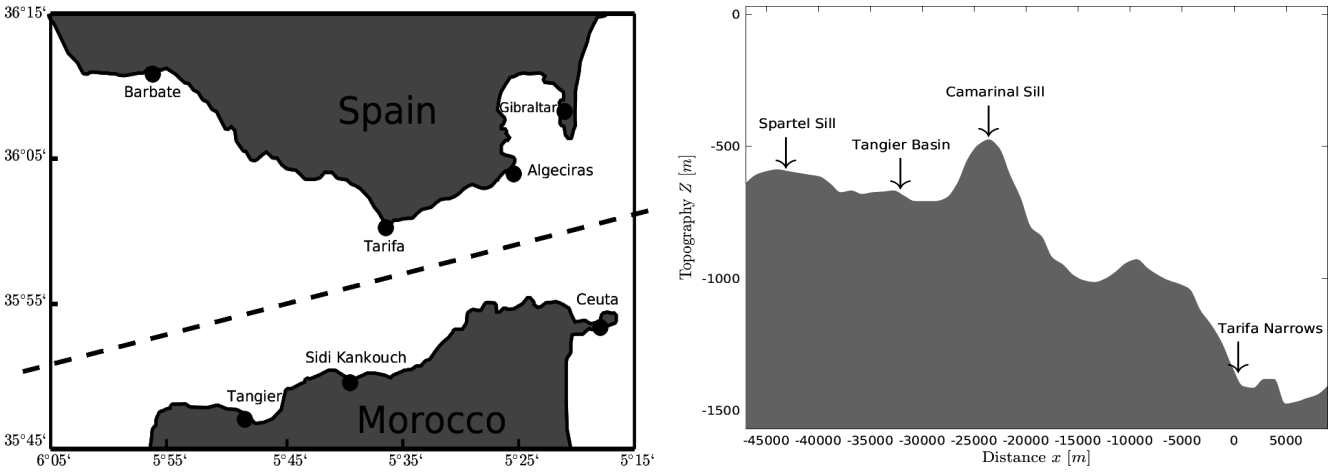

Figure 15: Schematic map of the Strait of Gibraltar along with relevant locations (left plot) and the bathymetry used for the one-dimensional simulations (right plot).

viscosity coefficient ν. It is clear that the velocity profile changes from straight to curved lines for small values of the viscosity coefficient. The convergence with respect to the number of layers can also be noted in the results presented in Figure 14. Weak exchange between the layers is expected for small values of the coefficient ν and this exchange becomes strong for large values of the coefficient ν. In addition, for small values of ν only one global recirculation is detected in the flow domain however, for $\nu > 0.01$ two local recirculations are detected in the domain. For these large values of the viscosity coefficient, the flow is reversed at the center of the hump and it forms two vertices recirculating at the left and right sides of the hump. It should also be stressed that the global discharge for the whole flow in this system is equal to zero but the local water discharge for each layer is not prescribed a priori. Furthermore, solving the multilayer system without mass exchange terms (*i.e.* $G = 0$ and $\nu = 0$) yields a flow at rest which is similar to the one obtained using the canonical single-layer model. Under the considered flow conditions, it has been shown that it is possible to resolve recirculation flow problems using only one global mass equation for the entire one-dimensional multilayer shallow water system.

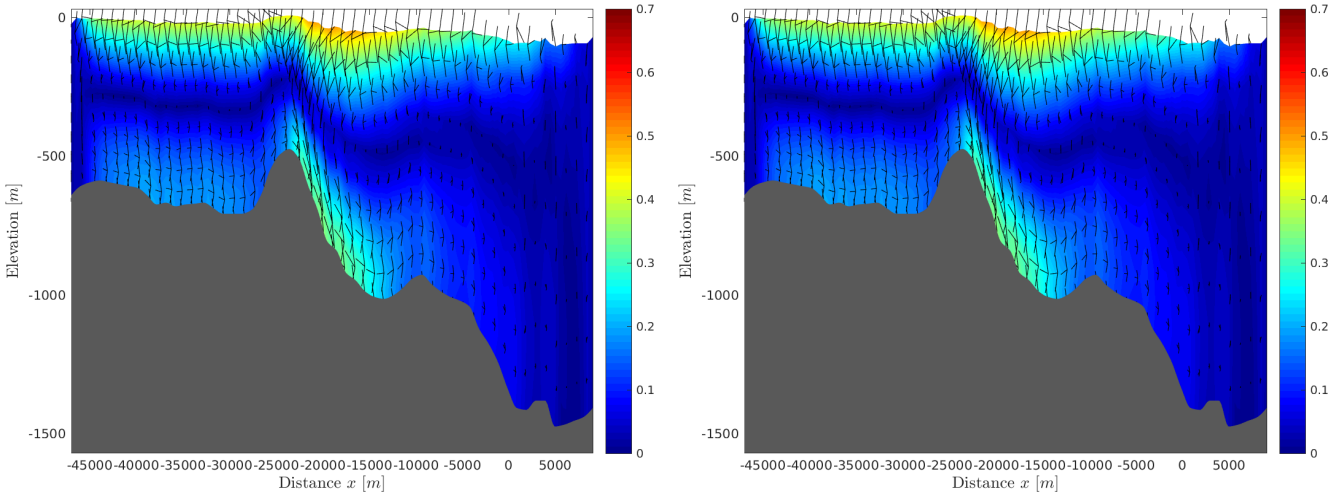

Figure 16: Distribution of the velocity fields for the recirculation flow problem in the Strait of Gibraltar using 10-layer model for a wind speed $w = 10\ m/s$ (left plot) and $w = 15\ m/s$ (right plot).

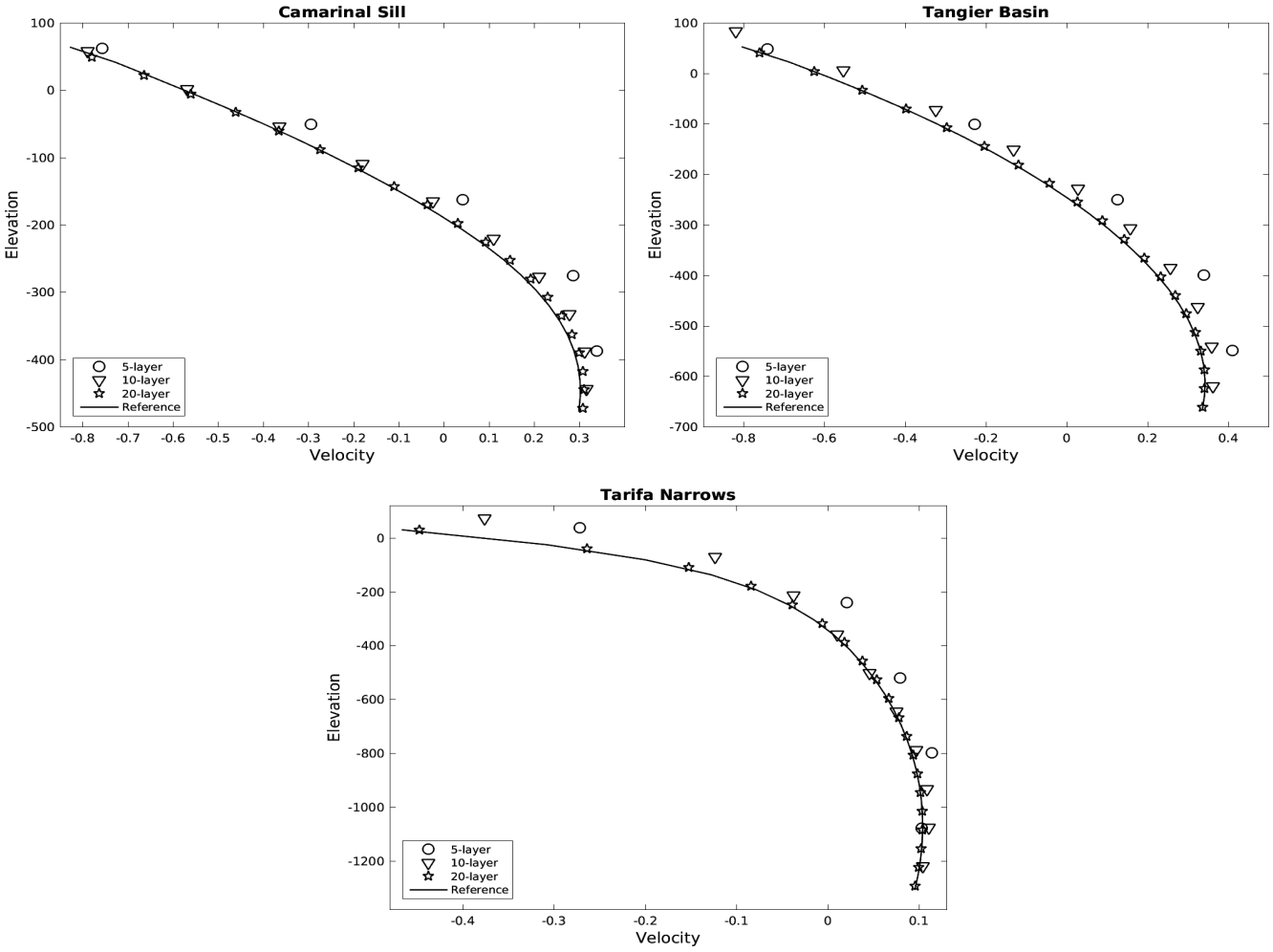

Figure 17: Velocity profiles at three different locations for the recirculation flow problem in the Strait of Gibraltar subject to a Levant wind with speed $w = 15\ m/s$ using different numbers of layers.

4.6 Recirculation flow problem in the Strait of Gibraltar

Our final test problem consists of a flow recirculation in the Strait of Gibraltar using the multilayer shallow water equations with mass exchange. Note that this flow problem presents a realistic practical test of multilayer shallow water flows for two major reasons. Firstly, the domain of the Strait of Gibraltar is large including high gradients of the bathymetry and well-defined shelf regions. Secondly, the Strait is deep and contains two water bodies with different densities, which present a challenge in the shallow water modelling. Indeed, the basic Oceanic circulation in the Strait of Gibraltar consists of an upper layer of cold, fresh surface Atlantic water and an opposite deep current of warmer, salty outflowing Mediterranean water, compare for example [3, 15, 26, 40]. A schematic map of the Strait of Gibraltar along with relevant locations is depicted in the left plot of Figure 15. The system is bounded to the north and south by the Iberian and African continental forelands, respectively, and to the west and east by the Atlantic ocean and the Mediterranean sea. In geographical coordinates, the Strait is $35^o45'$ to $36^o15'$ N latitude and $5^o15'$ to $6^o05'$ W longitude. Here, we consider a one-dimensional cross-section along the Strait (obtained by a longitudinal section along the dashed line in the left plot of Figure 15) subject to a Levant wind with speeds $w = 10\ m/s$ and $w = 15\ m/s$ blowing from the east to the west in the Strait. Initially, the system is at rest and the computational domain and the associated bathymetry are displayed in the right plot of Figure 15. This restricted domain has also been considered in [31] among others. In all simulations, we have used $\rho_a = 1200\ kg/m^3$, $g = 9.81\ m/s^2$, $\nu = 0.01\ m^2/s$, $n_b = 0.008\ s/m^{1/3}$,

$\sigma_s = 0.0015$, the computational domain is discretized into 50 elements, the degree of the polynomial approximation is set to $N = 3$ and numerical results are presented for 10 layers at time $t = 7.3$ *hours*. The purpose here is to assess the performance of the proposed RKDG method for a recirculation flow problem in the Strait of Gibraltar using multilayer shallow water equations. This step is very important if one wants to monitor the hydraulic linked activities such as maritime transport and fishery among others in the Strait of Gibraltar.

In Figure 16 we display the distribution of velocity intensities and fields obtained for the 10-layer model subject to a Levant wind with speeds $w = 10\ m/s$ and $w = 15\ m/s$. As expected, the blowing Levant wind generates two recirculation zones in the Strait separated by the Camarinal sill. In addition, a strong recirculation with high velocity intensities is generated for the blowing Levant wind with $w = 15\ m/s$ than with $w = 10\ m/s$ but in both cases high velocities have been detected near the bed topography in the right area behind the Camarinal sill. It should be stressed that these hydraulic effects can not be captured using the standard single-layer shallow water equations while using the three-dimensional Navier-Stokes equations would be computationally very demanding. The effect of number of layers on these recirculation flows has also been investigated for this problem and in Figure 17 we illustrate the velocity profiles obtained at three different locations in the Strait of Gibraltar. Here, we consider the Camarinal sill, Tangier basin and Tarifa narrows located at $x = -24\ Km$, $x = -32.5\ Km$ and $x = 0\ Km$, respectively. Results obtained using the multilayer model with 5, 10 and 20 layers are also compared to the reference results obtained using 50 layers and 500 elements for the considered locations. From the velocity profiles depicted in Figure 17, it is clear that high velocity intensities are appeared on the water free-surface compared to the bottom topography at all considered locations and the highest intensities are detected at the Camarinal sill. The effects of the bathymetry on these velocity profiles can also be seen in these results as more curved profile is obtained in the shallow zone at Tarifa narrows than in the deep zones at the Camarinal sill and Tangier basin. The convergence of the reference solutions as the number of layers is increased should also be noted in the results presented in Figure 17. The computational results demonstrate the capability of the proposed RKDG method that can provide insight to complex free-surface recirculation flows in large domain with irregular bathymetry.

5 Conclusions

A well-balanced Runge-Kutta discontinuous Galerkin method to solve multilayer free-surface flows with mass exchange has been presented. The equations have been reformulated in a large system of conservation laws with source terms accounting for the friction and momentum exchange effects. The inter-layer coupling in the flow system has been accounted for using a class of mass exchange terms between the water layers. The method combines some features of the finite element and finite volume solvers to yield an attractive method because of its formal high-order accuracy and its ability to resolve discontinuities without generating nonphysical oscillations. The proposed Runge-Kutta discontinuous Galerkin method can be interpreted as a stable locally conservative finite element solver whose approximate solutions are discontinuous across the inter-element boundaries. To preserve the well-balanced property, a special discretization of source terms is implemented based on the nature of hydrostatic solutions along with the Gauss-Lobatto-Legendre nodes for the quadrature used in the approximation of source terms. Numerical results and applications have been illustrated for several test problems of multilayer free-surface flows on both flat and non-flat beds. The presented results demonstrate the high accuracy of the Runge-Kutta discontinuous Galerkin method and its ability to simulate free-surface flows in the hydraulic regimes considered. Comparisons to three-dimensional results obtained for the hydrostatic incompressible Navier-Stokes equations and for a class of kinetic methods have also been included in this study. Results obtained for a recirculation flow problem in the Strait of Gibraltar have also been illustrated in this study. The presented results reveal good shock resolution with high accuracy in smooth regions and without any spurious oscillations near the shock areas. Although we have restricted our simulations to the one-dimensional problems, the well-balanced Runge-Kutta discontinuous Galerkin method

investigated in the current work can be extended to multilayer free-surface flows in two space dimensions with viscous terms, Coriolis forces and over complex topography. These and further issues are subject of future investigations. Finally, the method presented in this paper does not straightforwardly resolve we/dry areas in the multilayer shallow water flows. However, using ideas of wet/dry treatment developed in [30] for standard single-layer shallow water equations, it is possible to reconstruct an efficient wetting and drying treatment for two-dimensional multilayer shallow-water models using the Runge-Kutta discontinuous Galerkin method. Results on these techniques will be reported in future works.

Acknowledgment. N. Izem is deeply grateful to the ERC fund used within the framework of the European Project Deep Blue to support his visit to Heriot-Watt university at Edinburgh.

References

[1] M.B. Abbott. *Computational hydraulics: Elements of the theory of free surface flows.* Fearon-Pitman Publishers, 1979.

[2] V. Aizinger and C. Dawson. A discontinuous Galerkin method for two-dimensional flow and transport in shallow water. *Advances in Water Resources*, 25:67–84, 2002.

[3] J.I. Almazán, H. Bryden, T. Kinder, and eds G. Parrilla. *Seminario Sobre la Oceanografía Física del Estrecho de Gibraltar.* SECEG, Madrid, 1988.

[4] E. Audusse, F. Benkhaldoun, S. Sari, M. Seaid, and P. Tassi. A fast finite volume solver for multilayered shallow water flows with mass exchange. *Journal of Computational Physics*, 272:23–45, 2014.

[5] E. Audusse, F. Bouchut, M.O. Bristeau, R. Klein, and B. Perthame. A fast and stable well-balanced scheme with hydrostatic reconstruction for shallow water flows. *SIAM Journal on Scientific Computing*, 25:2050–2065, 2004.

[6] E. Audusse, M.O. Bristeau, B. Perthame, and J. Sainte-Marie. A multilayer Saint-Venant system with mass exchanges for shallow water flows. Derivation and numerical validation. *M2AN Math. Model. Numer. Anal.*, 45:169–200, 2011.

[7] A. Bermudez and M.E. Vázquez-Cendón. Upwind methods for hyperbolic conservation laws with source terms. *Journal of Computers & Fluids.*, 23:1049–1071, 1994.

[8] B. Cockburn, G. E. Karniadakis, and C.-W. Shu (eds.). *Discontinuous Galerkin methods. Theory, computation and applications.* Lecture Notes in Computational Science and Engineering, 11. Springer-Verlag, Berlin, 2000.

[9] B. Cockburn, S.Y. Lin, and C.-W. Shu. TVB Runge-Kutta local projection discontinuous Galerkin finite element method for conservation laws III: One-dimensional systems. *Journal of Computational Physics*, 84:90–113, 1989.

[10] R. Codina. Numerical solution of the incompressible Navier–Stokes equations with Coriolis forces based on the discretization of the total time derivative. *Journal of Computational Physics*, 148:467–496, 1999.

[11] F. Couderc, A. Duran, and J.P. Vila. An explicit asymptotic preserving low Froude scheme for the multilayer shallow water model with density stratification. *Journal of Computational Physics*, 343:235–270, 2017.

[12] C. Eskilsson and S. J. Sherwin. A triangular spectral/hp discontinuous Galerkin method for modelling 2D shallow water equations. *International Journal for Numerical Methods in Fluids*, 45:605–623, 2004.

[13] E.D. Fernández-Nieto, E.H. Koné, and T. Chacón. A multilayer method for the hydrostatic Navier-Stokes equations: A particular weak solution. *SIAM Journal on Scientific Computing*, 60:408–437, 2014.

[14] G.J. Gassner, A.R. Winters, and D.A. Kopriva. A well balanced and entropy conservative discontinuous Galerkin spectral element method for the shallow water equations. *Applied Mathematics and Computation*, 272:291–308, 2016.

[15] F. Gómez. The role of the exchanges through the Strait of Gibraltar on the budget of elements in western mediterranean sea: Consequences of humain-induced modifications. *Marine Pollution Bulletin.*, 46:685–694, 2003.

[16] J. Gula, V. Zeitlin, and F. Bouchut. Instabilities of buoyancy-driven coastal currents and their nonlinear evolution in the two-layer rotating shallow water model. Part 2. active lower layer. *Journal Fluid Mechanics.*, 665:209–237, 2010.

[17] M. Herty, N. Izem, and M. Seaid. Fast and accurate simulations of shallow water equations in large networks. *Journal of Computers & Mathematics with Applications*, 78:6:2107–2126, September 2019.

[18] J.S. Hesthaven. From electrostatics to almost optimal nodal sets for polynomial interpolation in a simplex. *SIAM J. Numer. Anal.*, 35:655–676, 1998.

[19] J.S. Hesthaven and T. Warburton. High-order nodal methods on unstructured grids. I. time-domain solution of maxwells equations. *Journal of Computational Physics*, 181(1):186–221, 2002.

[20] N. Izem, M. Seaid, I. Elmahi, and M. Wakrim. Discontinuous Galerkin method for two-dimensional bilayer shallow water equations. *Journal of Engineering Mathematics*, 96:1–21, 2016.

[21] N. Izem, M. Seaid, and M. Wakrim. A discontinuous Galerkin method for two-layer shallow water equations. *Journal of Mathematics and Computers in Simulation*, 120:12–23, 2016.

[22] C.-W. Shu J. Qiu. Runge-Kutta discontinuous Galerkin method using WENO limiters. *SIAM Journal on Scientific Computing*, 26:907–929, 2005.

[23] L. Krivodonova. Limiters for high-order discontinuous Galerkin methods. *Journal of Computational Physics*, 226:879–896, 2007.

[24] N. Krvavica. Re-evaluating efficiency of first-order numerical schemes for two-layer shallow water systems by considering different eigenvalue solutions. *Advances in Water Resources*, 137:103508, March 2020.

[25] E.J. Kubatko, J.J. Westerink, C. Dawson, and A. Buffa. *hp* discontinuous Galerkin methods for advection dominated problems in shallow water flow. *Journal of Computer Methods in Applied Mechanics and Engineering*, 196:437–451, 2006.

[26] J.G. Lafuente, J.L. Almazán, F. Catillejo, A. Khribeche, and A. Hakimi. Sea level in the Strait of Gibraltar: Tides. *Int. Hydrogr. Rev. LXVII.*, 1:111–130, 1990.

[27] G. Li, O. Delestre, and L. Yuan. Well-balanced discontinuous Galerkin method and finite volume WENO scheme based on hydrostatic reconstruction for blood flow model in arteries. *International Journal for Numerical Methods in Fluids*, 86(7):491–508, 2018.

[28] G. Li and Y. Xing. Well-balanced discontinuous Galerkin methods with hydrostatic reconstruction for the Euler equations with gravitation. *Journal of Computational Physics*, 352:445–462, 2018.

[29] J. Li, G. Li, S. Qian, J. Gao, and Q. Niu. A high-order well-balanced discontinuous Galerkin method based on the hydrostatic reconstruction for the Ripa model. *Adv. Appl. Math. Mech.*, 12:1416–1437, 2020.

[30] L. Li and Q. Zhang. Development of an efficient wetting and drying treatment for shallow-water modeling using the quadrature-free Runge-Kutta discontinuous Galerkin method. *International Journal for Numerical Methods in Fluids*, 93(2):314–338, 2021.

[31] J. Macías, C. Parés, and M.J. Castro. Improvement and generalization of a finite element shallow water solver to multi-layer systems. *International Journal for Numerical Methods in Fluids*, 31:1037–1059, 1999.

[32] S. Noelle, N. Pankratz, G. Puppo, and J.R. Natvig. Well-balanced finite volume schemes of arbitrary order of accuracy for shallow water flows. *Journal of Computational Physics*, 213:474–499, 2006.

[33] I. Ozgen, J. Zhao, D. Liang, and R. Hinkelmann. Urban flood modeling using shallow water equations with depth-dependent anisotropic porosity. *Journal of Hydrology*, 541:1165 – 1184, 2016.

[34] H. Ozmen-Cagatay and S. Kocaman. Dam-break flows during initial stage using swe and rans approaches. *Journal of Hydraulic Research*, 48(5):603–611, 2010.

[35] B. Perthame and C. Simeoni. A kinetic scheme for the Saint-Venant system with a source term. *CALCOLO.*, 38:201–231, 2001.

[36] S. Qian, G. Li, F. Shao, and Y. Xing. Positivity-preserving well-balanced discontinuous Galerkin methods for the shallow water flows in open channels. *Advances in Water Resources*, 115:172–184, 2018.

[37] J. Qiu, B.C. Khoo, and C.-W. Shu. A numerical study for the performance of the Runge-Kutta discontinuous Galerkin method based on different numerical fluxes. *Journal of Computational Physics*, 212:540–565, 2006.

[38] N.J. Shankar, H.F. Cheon, and S. Sankaranarayanan. Multilevel finite-difference model for three-dimensional hydrodynamic circulation. *Ocean Eng.*, 24:785–816, 1997.

[39] C.-W. Shu. Total variation diminishing time discretizations. *SIAM J. Sci. Stat. Comput.*, 9:1073–1084, 1988.

[40] L. Tejedor, A. Izquierdo, B.A. Kagan, and D.V. Sein. Simulation of the semidiurnal tides in the Strait of Gibraltar. *J. Geophysical Research.*, 104:13541–13557, 1999.

[41] S. Tu and S. Allibadi. A slope limiting procedure in discontinuous Galerkin finite element method for gas dynamics applications. *Journal of Numerical Analysis and Modeling.*, 2:163–178, 2005.

[42] K.R. Tubbs and F.T.C. Tsai. Multilayer shallow water flow using lattice Boltzmann method with high performance computing. *Advances in Water Resources.*, 32:1767–1776, 2009.

[43] Z. Wang, J. Zhu, and N. Zhao. A new robust high-order weighted essentially nonoscillatory scheme for solving well-balanced shallow water equations. *Adv. Appl. Math. Mech.*, 11:911–941, 2019.

[44] Y. Xing. Exactly well-balanced discontinuous Galerkin methods for the shallow water equations with moving water equilibrium. *Journal of Computational Physics*, 257:536–553, 2014.

[45] Y. Xing and C.-W. Shu. High order finite difference WENO schemes with the exact conservation property for the shallow water equations. *Journal of Computational Physics*, 208:3206–227, 2005.

[46] Y. Xing and C.-W. Shu. A new approach of high order well-balanced finite volume WENO schemes and discontinuous Galerkin methods for a class of hyperbolic systems with source terms. *Communications in Computational Physics*, 1:100–134, 2006.

[47] J. Yan, X. Deng, A. Korobenko, and Y. Bazilevs. Free-surface flow modeling and simulation of horizontal-axis tidal-stream turbines. *Journal of Computers & Fluids*, 158:157 – 166, 2017.

[48] S. Zhao, J. Ovadia, X. Liu, Y.T. Zhang, and Q. Nie. Operator splitting implicit integration factor methods for stiff reaction-diffusion-advection systems. *Journal of Computational Physics*, 230:5996–6009, 2011.

[49] H. Zhu, Y. Cheng, and J. Qiu. A comparison of the performance of limiters for Runge-Kutta discontinuous Galerkin methods. *Adv. Appl. Math. Mech.*, 5(3):365–390, 2013.